



**Time-Resolved Photoluminescence of  
InAs/GaInSb Quantum Well Lasers**

**THESIS**

**Michael R. McKay**

**AFIT/GAP/ENP/01J-02**

**DEPARTMENT OF THE AIR FORCE  
AIR UNIVERSITY**  
**AIR FORCE INSTITUTE OF TECHNOLOGY**

**Wright-Patterson Air Force Base, Ohio**

---

---

**APPROVED FOR PUBLIC RELEASE; DISTRIBUTION UNLIMITED.**

**20010925 271**

The views expressed in this thesis are those of the author and do not reflect the official policy or position of the United States Air Force, Department of Defense, or the U. S. Government.

**Time-Resolved Photoluminescence of InAs/GaInSb Quantum Well Lasers**

**THESIS**

Presented to the Faculty  
Department of Engineering Physics  
Graduate School of Engineering and Management  
Air Force Institute of Technology  
Air University  
Air Education and Training Command  
In Partial Fulfillment of the Requirements for the  
Degree of Master of Science in Applied Physics

Michael R. McKay, B.S.

May 2000

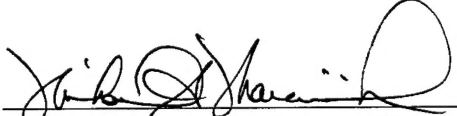
**APPROVED FOR PUBLIC RELEASE; DISTRIBUTION UNLIMITED.**

**AFIT/GAP/ENP/01J-02**

Time-Resolved Photoluminescence of InAs/GaInSb Quantum Well Lasers

Michael R. McKay, B.S.

Approved:

  
Lt. Col. Michael Marciniak (Chairman)

1 Jun 01  
date

  
Robert Hengehold (Member)

1 Jun 01  
date

  
David Weeks (Member)

1 Jun 01  
date

## **Acknowledgments**

I would like to express my sincere appreciation to my faculty advisor, Lt. Col. Michael Marciniak, for his guidance and support throughout the course of this thesis effort. Their insight and experience were certainly appreciated.

Michael McKay

## **ABSTRACT**

In the world of semiconductor photonic device fabrication, one important objective may be to extract as much light as possible from the device. In these devices, photons are created when electrons recombine with holes by transitioning from a high-energy state to a lower one. Unfortunately, electron-hole recombination does not always result in the formation of a photon. There are three basic types of recombination: the first results in the formation of a photon and is called radiative recombination; and the second and third, known as Shockley-Read-Hall and Auger recombination, result in the heating of the device and do not produce photons and are therefore called non-radiative recombination. All three processes occur simultaneously in a device, and either a radiative or non-radiative recombination coefficient can be associated with the relative rate of each. The lifetime of an electron in a high-energy state is so small, on the order of nanoseconds, that there is no way to measure these coefficients directly. However, sum frequency generation is a technique to indirectly measure these coefficients by taking advantage of the speed of light to resolve these processes in time. From the resulting data, these recombination coefficients can be extracted.

## TABLE OF CONTENTS

<b>1.</b>	<b>Introduction.....</b>	<b>1</b>
<b>2.</b>	<b>Background.....</b>	<b>4</b>
2.1.	The Bandgap.....	4
2.2.	Density of States.....	6
2.3.	Heterojunctions and Quantum Wells.....	8
2.4.	Electron and Hole Quantum Well Confinement.....	9
2.5.	Electron-Hole Recombination in Mid-Infrared Semiconductors.....	11
2.6.	Non-Radiative Recombination.....	11
2.7.	Radiative Recombination.....	12
<b>3.</b>	<b>Literature Review.....</b>	<b>14</b>
3.1.	III-V Mid-Infrared Ternary Semiconductor Lasers.....	14
3.2.	Projects Utilizing Sum Frequency Generation.....	17
<b>4.</b>	<b>Experimental Setup.....</b>	<b>21</b>
4.1.	The Setup.....	21
4.2.	Upconversion Technique.....	25
4.3.	Zero Path Length.....	26
4.4	Time-Resolved Photoluminescence.....	28
4.5	Analysis.....	29
4.5.1	Curve Fitting.....	31
4.6	Samples Studied.....	32
<b>5.</b>	<b>Results and Analysis.....</b>	<b>33</b>
5.1.	Photoluminescence Results .....	33

5.2. TRPL Data.....	34
5.3. Individual Curve Fitted TRPL Data.....	35
5.3.1. Individual Curve Fits for Sample 90.....	35
5.3.2. Individual Curve Fits for Sample 91.....	37
5.4. Representative Recombination Coefficients.....	42
5.5. Summary.....	46
<b>6. Conclusions and Future Work.....</b>	<b>48</b>
6.1. Future Work.....	48
<b>Appendix A.....</b>	<b>50</b>
<b>Appendix B.....</b>	<b>55</b>
<b>Bibliography.....</b>	<b>65</b>
<b>Vita.....</b>	<b>67</b>

## LIST OF FIGURES

Figure 2-1: Band formation as single Silicon atoms are brought together to form a crystalline lattice after McKelvey (1993).....	5
Figure 2-2: Density of States(a), Fermi-Dirac Distribution(b), and Carrier Concentrations for and intrinsic(undoped) semiconductor after McKelvey (1993).....	6
Figure 2-3: (a)Two different materials with bandgaps $E_{g1}$ and $E_{g2}$ . (b)Resulting band structure when one material is grown on the other. (c)Formation of multi quantum wells by alternate growth of materials 1 and 2 After Bhattacharya (1997).....	7
Figure 2-4: Three basic categories for heterojunctions. Type I(a), Type IIa(b), and Type IIb(c) after Bhattacharya (1997).....	8
Figure 2-5: Solutions to Schrodinger's wave equation. Satisfying the transcendental equations results in discrete energy levels in the wells after Gasiorowitz (1998).....	10
Figure 2-6: Graphical representation of Photoluminescence in single crystal semiconductor material.....	13
Figure 3-1: Atmospheric Transmission Window and related band-gap vs. lattice parameter for III-V semiconductor compounds and their alloys after Marciniak(1995).....	15
Figure 4-1: Experimental setup of the upconversion experiment after Cooley (1997).....	22
Figure 4-2: Autocorrelation of mode-locked Ti:Sapphire laser.....	23
Figure 4-3: Graphical representation of momentum conservation within nonlinear crystal.....	27
Figure 4-4: Excitation pulse and luminescence decay as a function of time (a). Delayed laser pulse $\tau$ ps away from zero path length(b).....	29
Figure 4-5: Configuration of samples 90 and 91.....	32
Figure 5-1: Photoluminescence of samples 90 and 91 at 77 K and 5.5 K.....	34
Figure 5-2: Raw upconversion data upconversion data for sample 90 at 77 K.....	35
Figure 5-3: Raw upconversion data upconversion data for sample 90 at 5.5 K.....	35

Figure 5-4: Raw upconversion data upconversion data for sample 91 at 77 K.....	35
Figure 5-5: Raw upconversion data upconversion data for sample 90 at 5.5 K.....	35
Figure 5-6: Conversion from upconversion to carrier density for samples 90 and 91 at 77 K and 5.5 K.....	36
Figure 5-7: Best individual curve fits for sample 90 at 77 K.....	38
Figure 5-8: Best individual curve fits for sample 90 at 5.5 K.....	39
Figure 5-9: Best individual curve fits for sample 91 at 77 K.....	40
Figure 5-10: Best individual curve fits for sample 90 at 5.5 K.....	41
Figure 5-11: Curve fits with representative coefficients for sample 90 at 77 K.....	42
Figure 5-12: Curve fits with representative coefficients for sample 90 at 5.5 K.....	43
Figure 5-13: Curve fits with representative coefficients for sample 91 at 77 K.....	44
Figure 5-14: Curve fits with representative coefficients for sample 91 at 5.5 K.....	45

## LIST OF TABLES

Table 1-1: Recombination coefficients for samples 90 and 91 at 77 K and 5.5 K.....	3
Table 3-1: Radiative and nonradiative coefficients for sample A and B at 77 and 150 K after Cooley (1997).....	19
Table 5-1: Individual coefficients for sample 90 at 77 K.....	38
Table 5-2: Individual coefficients for sample 90 at 5.5 K.....	39
Table 5-3: Individual coefficients for sample 91 at 77 K.....	40
Table 5-4: Individual coefficients for sample 91 at 5.5 K.....	41
Table 5-5: Representative recombination coefficients for samples 90 and 91 at 77 K and 5.5 K.....	47
Table 5-6: Recombination coefficients obtained by Cooley (1997).....	47
Table 6-1: Recombination coefficients for samples 90 and 91 at 77 K and 5.5 K.....	48

## **1. Introduction**

Because of their light weight and compact size, semiconductor lasers are in use in a variety of commercial and government areas. Specifically, lasers that emit in the mid-infrared (mid-IR) range have been applied to laser radar, remote sensing of gases (Choi, 1996), molecular spectroscopy, and laser medicine. In particular, the Air Force is interested in mid-IR semiconductor lasers for use as infrared countermeasures (IRCM). Since heat seeking missiles detect targets by their infrared signatures, a mid-IR semiconductor laser may be able to confuse or destroy the detection system, rendering the missile ineffective.

When fabricating semiconductor lasers for these applications, it is desirable to extract as much light out of these devices as possible. However, the production of light is only one of three recombination processes that take place within a semiconductor laser. The first process, known as Shockley-Read-Hall recombination (SRH), is a non-radiative process resulting in the heating of the device. The second process, known as radiative recombination, is a radiative process resulting in the production of a photon. The third process, known as Auger recombination, is a non-radiative process also resulting in the heating of the device. When fabricating photonic devices, one wants to maximize the radiative process and minimize the non-radiative processes. These three processes can be related to a rate at which carrier density is depleted from the higher energy state. This relation takes the form

$$-\frac{dn}{dt} = A_{SRH} n + B_{rad} n^2 + C_{Auger} n^3, \quad (1-1)$$

where  $n$  is the carrier density,  $A_{SRH}$ ,  $B_{rad}$ , and  $C_{Auger}$  are the SRH, radiative, and Auger recombination coefficients respectively.

The goal of this thesis is to determine these coefficients; however, they cannot be measured directly since they occur on nanosecond time scales. Therefore, an indirect method must be used. Time-Resolved Photoluminescence (TRPL) is an indirect means of determining these coefficients. It employs Sum Frequency Generation (SFG), which takes advantage of the speed of light in order to resolve these processes in time.

Typically, mid-IR semiconductor lasers take the form of a Type I quantum well structure. A Type I structure can be described as having the electron and hole wells in the same material. The samples investigated in this thesis were InAs/GaInSb-based lasers that take the form of a Type II structure. A Type II structure can be described as having the electron and hole wells in different materials. Type II structures are believed to have a lower Auger contribution to the recombination process than Type I since performance of Type I structures significantly decreases at higher temperatures while the Auger processes significantly increase with temperature.

TRPL was performed on two samples, which were virtually identical except for the InAs thickness, at liquid nitrogen and liquid helium temperatures. The TRPL data was then curve fit to the solution of Equation 1-1 and the coefficients were extracted. The final results are presented in Table 1-1.

Sample	Temp (K)	$A_{SRH}^{-1}$ (ns)	$B_{rad}$ (cm <sup>3</sup> /sec)	$C_{Auger}$ (cm <sup>6</sup> /sec)
90	77	1.19	7.73E-12	3.37E-32
90	5.5	2.72	4.52E-11	2.91E-30
91	77	6.65	2.30E-11	9.21E-31
91	5.5	10.7	1.00E-11	2.90E-31

Table 1-1: Recombination coefficients for samples 90 and 91 at 77 K and 5.5 K.

## **2.Background**

The purpose of this chapter is to provide a basic background to properties, characteristics and behavior of semiconductors. The bandgap of semiconductors, which is one of the most important parameters of such materials, will be described, as well as how it leads to the formation of structures such as double heterostructures, quantum wells (QW), and superlattices. The chapter will then briefly discuss band-to-band recombination dynamics. This chapter assumes that the reader has some basic knowledge of the quantum mechanical properties of atoms; therefore there will not be any derivations of equations or formulas.

### **2.1. The Bandgap**

When one studies the quantum mechanical behavior of atoms, it is learned that electrons belonging to any one atom have discrete energies. These discrete energies represent the allowed energies, or energy levels, that the electron may have. A characteristic of these energy levels is that the difference between adjacent levels decreases as the energy of the level increases. Figure 2-1 shows the discrete energy levels of the lower energy electrons for a single silicon atom.

However, when these single atoms are brought together to form a crystalline solid, the energy levels begin to split to form energy bands. Refer to Figure 2-1. The atoms eventually reach a position with respect to the other atoms at which their total energy is minimized. In this state of minimum energy, the atoms form a crystalline

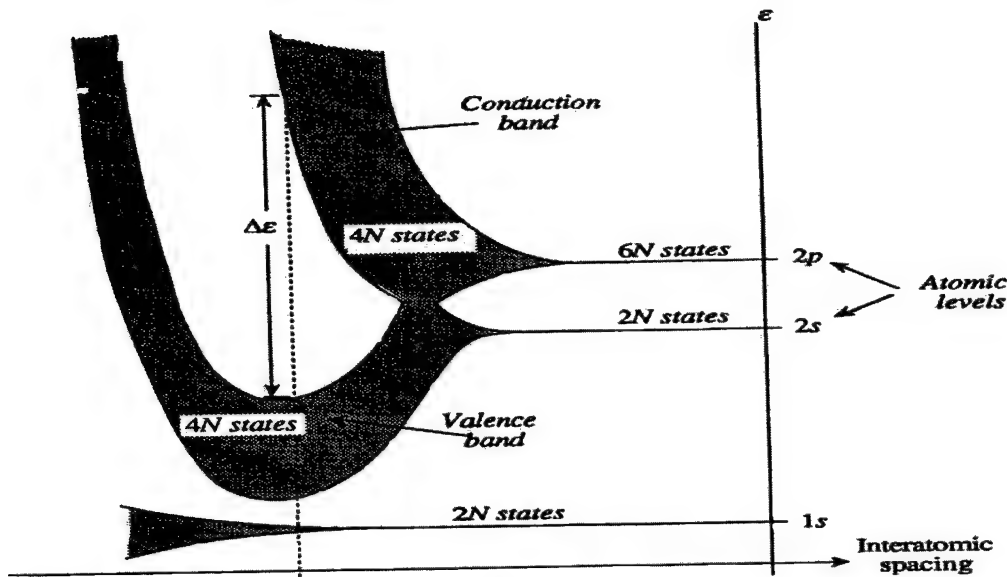


Figure 2-1: Band formation as single Silicon atoms are brought together to form a crystalline lattice after McKelvey (1997).

solid where the distance between atoms is referred to as the lattice constant,  $a_0$ . In this crystalline form, the allowed electron energies take on the form of bands separated by an energy gap. The bottom band is referred to as the valence band and the top band is referred to as the conduction band. The valence band is defined as the upper-most band that is completely full of electrons at  $T = 0$  K and the conduction band is defined as the lowest band that is completely empty at  $T = 0$  K. At temperatures above 0 K, the valence band becomes ‘almost full’ while the conduction band becomes ‘almost empty’. Within these bands, the electron energies are continuous, not discrete. The energy gap between the conduction and valence bands,  $\Delta\epsilon$ , is the bandgap. Within the bandgap, there are no allowed electron energy levels. For simplicity, the bandgap is often presented as two horizontal lines representing the bottom of the conduction band ( $E_c$ ) and the top of the valence band ( $E_v$ ) as in Figure 2-2a

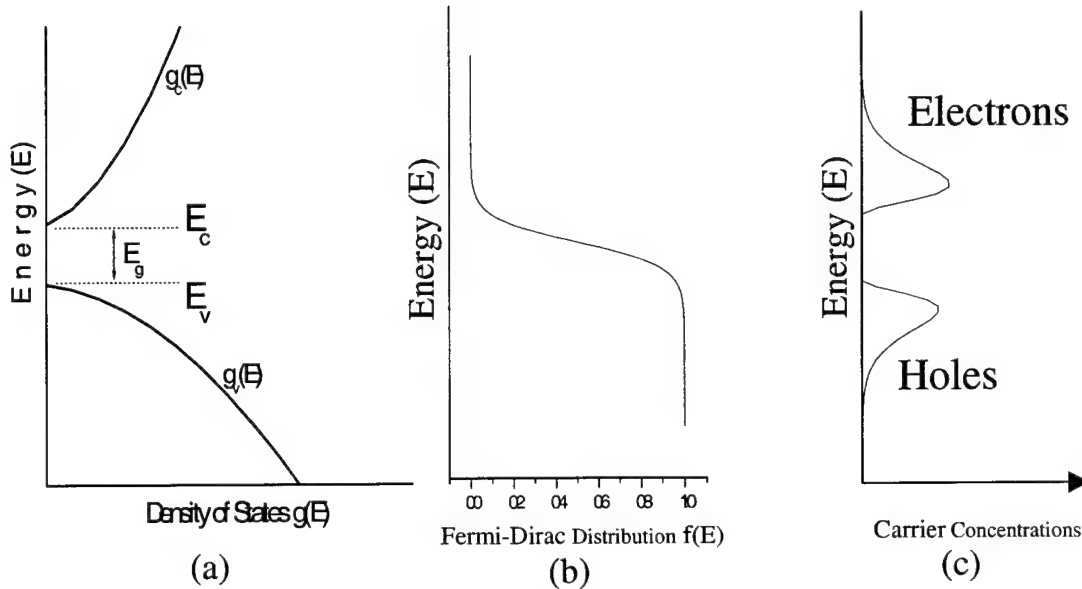


Figure 2-2: Density of States (a), Fermi-Dirac Distribution (b), and Carrier Concentrations for an intrinsic (undoped) semiconductor (c) after McKelvey (1993).

## 2.2. Density of States

The conduction and valence bands represent a continuum of allowed electron energies. However, there are a specific number of electrons that can have the same energy. This is referred to as the density of states, which states that there is a certain quantity of electrons for a given energy. Figure 2-2a shows a typical density of states for the conduction and valence bands. The density of states describes the number of available states but does not reveal which states are occupied. The density of states for electrons in the conduction band is given by

$$g_c(E) = \frac{8\sqrt{2\pi}}{h^3} m_c^{3/2} \sqrt{E - E_c}, \quad (2-1)$$

where  $m_c^*$  is the effective mass of the electron in the conduction band, and  $E_c$  is the energy of the conduction band. The density of states for the holes in the valence band is given by

$$g_v(E) = \frac{8\sqrt{2\pi}}{h^3} m_v^{*3/2} \sqrt{E_v - E}, \quad (2-2)$$

where  $m_v^*$  is the effective mass of the hole in the valence band, and  $E_v$  is the energy of the valence band. The Fermi-Dirac function (Figure 2-2b) gives the probability that a state is occupied and, when combined with the density of states, will yield the density of occupied states (Figure 2.-2c). The Fermi-Dirac function is given by

$$f(E) = \frac{1}{1 + e^{(E-E_f)/KT}}, \quad (2-3)$$

where  $E_f$  is the fermi energy, which is half the bandgap energy for an intrinsic material.

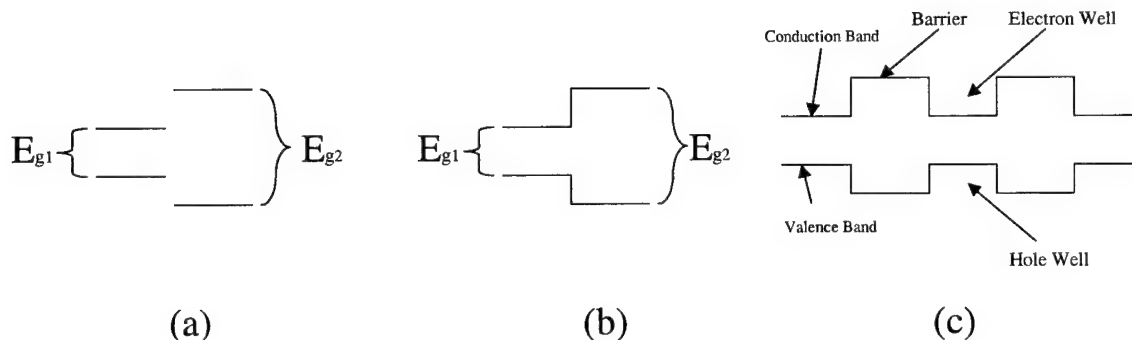


Figure 2-3: (a)Two different materials with bandgaps  $E_{g1}$  and  $E_{g2}$ . (b)Resulting band structure when one material is grown on the other. (c)Formation of a double heterojunction by alternate growth of materials 1 and 2.

### 2.3. Heterojunctions and Quantum Wells

Devices today, such as laser diodes and light emitting diodes (LED's), are not fabricated from just one single semiconductor material or semiconductor alloy consisting of one bandgap, but from a series of different semiconductors and alloys. One of the goals when fabricating these devices is to confine the electrons and holes in space. This confinement is accomplished by growing two different semiconductors, or two different semiconductor alloys, together, which have different associated bandgaps (Figure 2-3a). The result is a heterojunction, which is represented by an abrupt change in the energy of the conduction and valence bands in the direction of growth (Figure 2-3b). By repeating the growth process, one can create a double heterojunction, which has a region of electron and hole confinement (Figure 2.3c). This confinement is commonly referred to

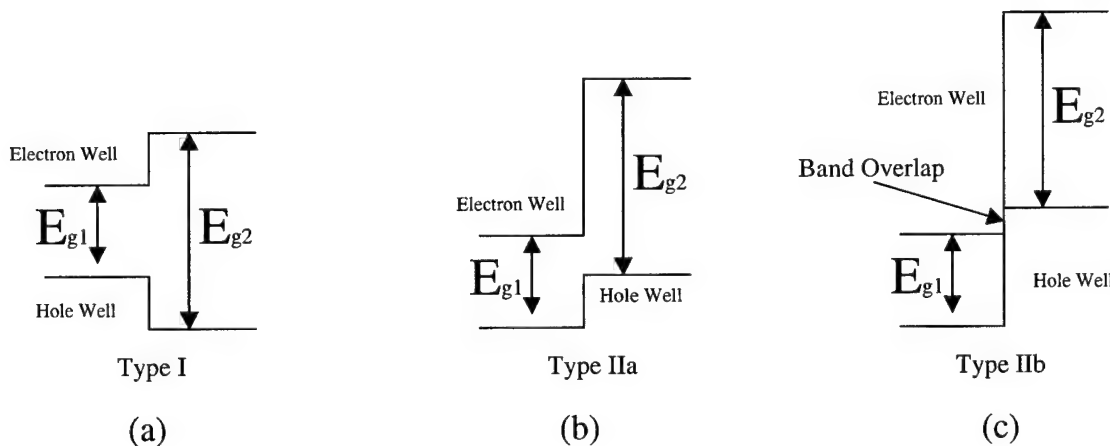


Figure 2-4: Three basic categories for heterojunctions. Type I(a), Type IIa(b), and Type IIb(c) after Bhattacharya (1997).

as a well. Electrons in the conduction band can ‘fall’ into the well, while the holes in the valence band can ‘rise’ into the well and become confined. When the width of the well becomes small, on the order of a few hundred angstroms, the confined electron and hole energies become quantized and the well is referred to as a quantum well. The quantized energy levels will be discussed in section 2.4.

All heterojunctions, and therefore quantum wells, fall into three basic types (Figure 2-4). The type I structure (Figure 2-4a) has a definite well for both electrons and holes. These wells completely overlap in space. The type IIa structure (Figure 2-4b) also has a definite well for both electrons and holes but they no longer overlap in space; the wells are staggered. The type IIb structure (Figure 2-4c) has its wells staggered, as well, but now the conduction and valence bands overlap in energy. Double heterostructures constructed from type IIb band structures are sometimes referred to as superlattices.

#### **2.4. Electron and Hole Quantum Well Confinement**

Confinement of electrons and holes, or carriers, is accomplished using quantum wells. The question now is, “What is the behavior of these carriers when they become confined?” Quantum mechanics says to solve Schrodinger’s time-independent wave equation for a one-dimensional finite potential well in order to determine the energies of these carriers. The solution to the wave equation reveals, in the form of transcendental equations, that the energies of the confined carriers in the wells are, once again, discrete.  $\Psi$  represents the wave function of the carrier, E is the energy of the carrier, m is the mass of the carrier,  $V_0$  is the depth of either the electron or hole well, and L is the width of the

wells. There is a finite number of energies that the carriers can have for each well depending on the various parameters such as well depth and well width (Figure 2-5). However, regardless of the size of the well, there will always be at least one confined state within a well. This simple calculation for predicting the number and energy of the allowed states within a well works for both Type I and Type IIa heterostructures. However, this prediction breaks down for Type IIb structures due to the band overlap. There is a method to try to predict the confined energy levels in Type IIb structures. It is known as  $k \bullet p$ , the specifics of which are well beyond the scope of this thesis.

In summary, the discrete energy levels within an atom lead to the formation of continuous energy bands when these atoms form crystalline lattices. Manipulation of these bands then give rise to electron and hole confinement structures. Within these structures the electrons and holes can again have discrete energy levels.

#### One-Dimensional Time-Independent Schrodinger's Wave Equation

$$\frac{d^2\Psi}{dx^2} = \frac{2m(V_o-E)\Psi}{\hbar^2}$$

#### Transcendental Equations

$$k\tan(kL/2) = (\alpha^2 - k^2)^{-1/2}$$

$$-k\cot(kL/2) = (\alpha^2 - k^2)^{-1/2}$$

$$\alpha^2 = 2mV_o/\hbar^2$$

$$k^2 = 2mE/\hbar^2$$

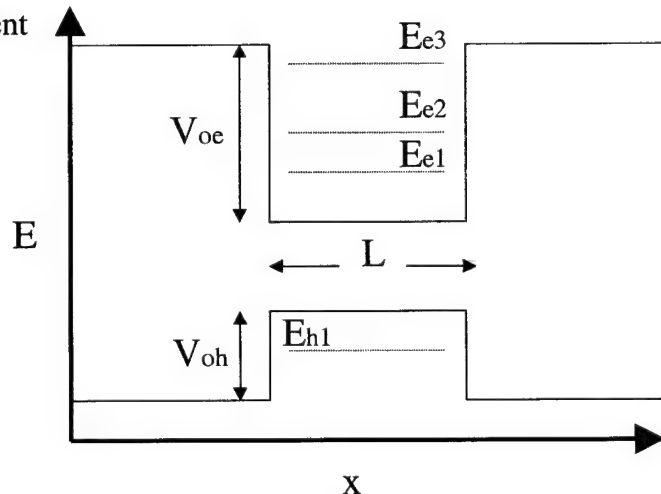


Figure 2-5: Solutions to Schrodinger's wave equation. Satisfying the transcendental equations results in discrete energy levels in the wells.

## **2.5 Electron-Hole Recombination in Mid-Infrared Semiconductors**

Recombination refers to when an electron makes a transition from a high-energy state, i.e., one of the discrete energy levels in the electron well, to a low-energy state, i.e., one of the discrete, empty energy levels in the hole well. These structures help confine electrons and holes in the hopes that these carriers will recombine and produce a photon. However, the recombination of carriers does not always result in the formation of a photon. In fact, there are three basic recombination processes. The first results in the formation of a photon, with energy equal to the difference in energy between the high and low energy states, which is referred to as radiative recombination. The second and third, known as Shockley-Read-Hall (SRH) and Auger recombination, result in the heating of the device, do not produce photons, and are therefore referred to as non-radiative recombination. All three processes occur simultaneously in a device, and either a radiative recombination coefficient,  $B_{rad}$ , or non-radiative recombination coefficient,  $A_{SRH}$  or  $C_{Auger}$ , can be associated with the relative rate of each. The relationship between these coefficients and the density of electrons,  $n$ , in the high-energy state is often represented by the rate equation below.

$$-\frac{dn}{dt} = A_{SRH}n + B_{rad}n^2 + C_{Auger}n^3 \quad (2-4)$$

## **2.6 Non-Radiative Recombination**

SRH recombination occurs when an electron recombines with a hole, giving up its energy in the form of one or more phonons. Phonons are lattice vibrations and lead to heating of the device. Usually, heating is undesirable in photonic devices because

thermal energy can decrease the bandgap of materials, which can change the properties of the device.

Auger recombination represents a transition in which an electron recombines with a hole, giving up its energy to another electron in the split-off band. This electron transitions to another hole state in the valence band. The hole in the split-off band is then left to thermalize, giving off its energy to the lattice. Transitions involving the transfer of energy to the split-off band are dominant in mid-infrared devices because the energy difference between the split-off band and the light-hole band is comparable to the bandgap.

## 2.7. Radiative Recombination

Carrier recombination resulting in the formation of a photon is referred to as radiative recombination. Radiative recombination can be observed by performing photoluminescence experiments. Photoluminescence is performed by optically exciting a sample via a laser (Figure 2.6). The sample absorbs a photon from the laser via the excitation of the electrons in the valence band up to the conduction band. These electrons are excited high in the conduction band and immediately try to minimize their energy by ‘cooling’ down to the minimum of the band. This ‘cooling’ is the electron’s way of giving off energy in the form of phonons. Once the electrons reach the minimum of the band, they recombine down to the valence band, giving up its energy in the form of a photon. As mentioned in section 2.5, the electron can also recombine nonradiatively, but in photoluminescence, only radiative recombination is observed and measured.

The lifetime of an electron in a conduction band is so small, on the order of nanoseconds, that there is no way to measure the recombination coefficients directly. That is where time-resolved photoluminescence (TRPL) comes into play. TRPL is a technique that employs sum frequency generation (SFG), which allows one to measure the radiative and nonradiative coefficients indirectly. SFG takes advantage of the speed of light to resolve these recombination processes in time. Chapter 4 will go into detail of TRPL using SFG.

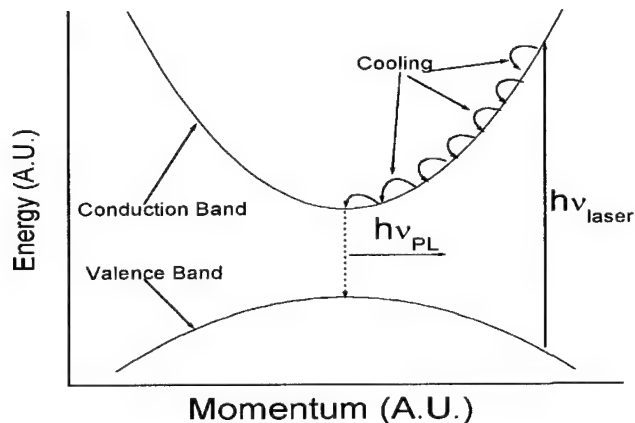


Figure 2-6: Graphical representation of Photoluminescence in single crystal semiconductor material.

### **3.Literature Review**

This chapter will cover a brief, current literature review on previous research efforts on  $\text{Ga}_{1-x}\text{In}_x\text{Sb}$  and other related III-V ternary semiconductor materials for use in mid-infrared laser fabrication. It has been divided into two sections. The first will provide a background on the III-V mid-infrared laser research. The second will give a synopsis on the technique of sum frequency generation (SFG), sometimes referred to as upconversion. Sections 3.1 and 3.2 will be presented in a chronological manner.

#### **3.1. III-V Mid-Infrared Ternary Semiconductor Lasers**

Ternary alloys, materials consisting of three different III-V semiconductors, that emit light in the range of 1 to 5 microns are very attractive in a wide range of applications. Such applications include remote sensing of atmospheric gasses, molecular spectroscopy, telecommunications, and laser radar. The Air Force is particularly interested in mid-infrared semiconductor lasers for use in infrared counter measures (IRCM). Figure 3.1 shows atmospheric transmission as a function of wavelength, as well as possible corresponding ternary alloys that may emit light at those wavelengths. The areas of high transmission, or windows, are of interest since these wavelengths can propagate through the atmosphere with minimum absorption. Ternary alloys such as InGaAs, InAsP, InAsSb, and GaInSb, when used to fabricate laser devices, may be able to take advantage of these windows.

In 1995, Turner *et al.* reported emission wavelengths of  $3.9 \mu\text{m}$  from quantum well lasers operating in continuous wave (cw) mode up to 123K. These laser structures,

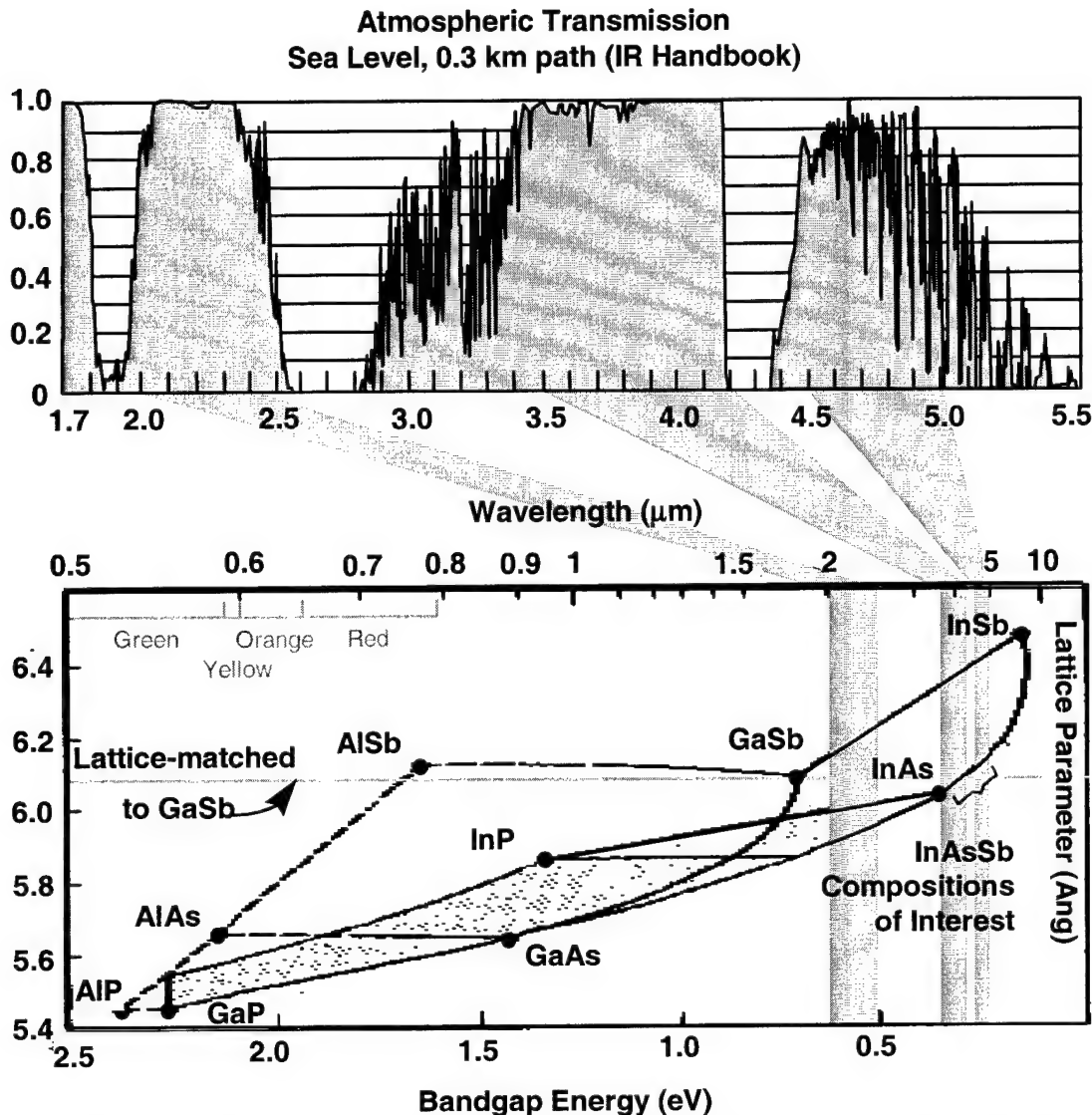


Figure 3-1: Atmospheric Transmission Window and related band-gap vs. lattice parameter for III-V semiconductor compounds and their alloys after Marciniak(1995).

grown via molecular-beam epitaxy (MBE), consisted of wells fabricated from  $\text{InAs}_{0.86}\text{Sb}_{0.14}$  and barriers fabricated from  $\text{In}_{0.85}\text{Al}_{0.15}\text{As}_{0.86}\text{Sb}_{0.14}$ . They were also able to obtain emission wavelengths as long as 4.5  $\mu\text{m}$  by substituting InAlAs for InAlAsSb as the barriers in the laser structures.

Oohashi *et al.* (1995) reported emission wavelengths of 1.3  $\mu\text{m}$  from  $\text{InAs}_{0.52}\text{P}_{0.48}$ -based, multiple-quantum-well (MQW) laser diodes. These laser diodes, grown via

chemical beam epitaxy (CBE), were able to operate CW up to 423 K. 1.3- $\mu$ m emission is of interest since that wavelength experiences minimum dispersion within fiber optic lines.

Chow *et al.* (1995) investigated GaInSb/InAs superlattices for use as infrared diode lasers. Their diodes were grown via MBE. By varying the thickness of the wells they were able to obtain laser emission wavelengths from 3.28  $\mu$ m, at 170 K, to 3.90  $\mu$ m, at 84 K.

Lane *et al.* (1996) grew InAs/InAsSb MQW lasers via metal-organic chemical vapor deposition (MOCVD). These lasers operated at 3.6  $\mu$ m at 90 K in pulse mode and could deliver up to 1 Watt (W) of power from both facets.

Almuneau *et al.* (1999) also studied GaInSb based MQW's as the active region for vertical cavity surface emitting lasers (VCSEL). They fabricated GaInSb/AlGaAsSb strained quantum well semiconductor lasers that operated at 1.55  $\mu$ m at room temperature. 1.55- $\mu$ m emission is of particular interest since that wavelength experiences minimum absorption in fiber optic lines.

Zhang *et al.* (2000) investigated the dynamic response of  $In_{0.5}Ga_{0.5}As/GaAs$  quantum dots. These quantum dots were grown using a cycled submonolayer approach demonstrated by Huffaker *et al.* These quantum dots emitted from 1.21 to 1.31  $\mu$ m over a range of 11 to 300 K. The specifics of the dynamic portion of the experiment will be discussed in the next section.

In that same year, Kuang *et al* grew InGaAs-InGaAlAs-InP diode lasers via solid-source MBE. They were using the well developed technology for InP-based lasers which emit at 1.55  $\mu$ m. The significance for that wavelength was already mentioned above. Kunag's diode lasers operated at wavelengths as long as 2.12  $\mu$ m in CW mode at 300 K.

These are just a handful of the many groups involved in the fabrication of mid-infrared semiconductor lasers, as well as just a few of the possible attainable wavelengths.

### **3.2. Projects Utilizing Sum Frequency Generation**

The technique of sum frequency generation, sometimes referred to as upconversion, involves the mixing of two different wavelengths within a nonlinear crystal to produce a third wavelength. The signal produced by the third wavelength directly corresponds temporally to the signal that is being upconverted. This technique will be discussed in further detail in Chapter 5.

The technique of sum frequency generation, or upconversion, was first exhibited by Mahr and Hirsch in 1974. They wanted to demonstrate that such a technique could deliver picosecond optical resolution. They mixed a 20-ps pulse from a tunable, continuously mode-locked, dye laser with, first, a mode-locked argon-ion laser, then with the luminescence from Rhodamine 6G within an ADP crystal. By mixing the dye laser with itself, or autocorrelation, they were able to determine pulse width.

It would be difficult to discuss upconversion without citing the paper by Jagdeep Shah (1988). In his paper, he covers everything from phase matching to collection and detection of the upconverted signal. It truly is the handbook of upconversion.

However, it was not until 1989 that upconversion was first used to determine radiative and Auger recombination coefficients in GaSb by Snow et al. (1989).

In that same year, Heyen *et al.* (1989) applied the upconversion technique to determine radiative recombination rates in PbTe quantum wells. They determined that

the recombination rate varied approximately as  $1/T$ , where  $T$  was the temperature in Kelvin, for an assumed two-dimensional carrier density. They did not convert their upconversion signal to a three-dimensional carrier density, nor did they obtain quantitative values for either the radiative or non-radiative rates.

Hausser *et al.* (1990) reported on the Auger recombination coefficient ( $C_{\text{Auger}}$ ) of bulk InGaAs and InGaAs/InP QW's using time-resolved photoluminescence (TRPL). Their experiment consisted of a mode-locked, Q-switched Nd:YAG laser with a pulse width of about 150 ps. They measured  $C_{\text{Auger}}$  to be  $3.2 \times 10^{-28} \text{ cm}^6/\text{s}$  for bulk InGaAs at room temperature and  $0.9 \times 10^{-28} \text{ cm}^6/\text{s}$  for 11.nm wide InGaAs QW's, regardless of temperature.

Qian *et al.*(1993) performed TRPL on InGaAs/GaAs single quantum wells in order to study their temporal properties at 77 K. They focused on the behavior of radiative and nonradiative lifetimes, rather than the recombination coefficients, as a function of excitation power, well composition, and well width. Their experiment consisted of an active mode-locked Nd:YAG laser, in which the second harmonic generated beam pumped a dye laser and produced 12-ps pulses. They concluded that both lifetimes were affected by temperature, well thickness, and In content within the well. They also observed shorter lifetimes for larger well widths.

McCahon *et al* (1996) investigated the recombination dynamics in (GaInSb/InAs)/AlGaSb superlattices. They employed time-resolved differential transmission, which is a technique that measures the transmission through a sample, rather than emission, as a function of time. They were able to determine the Shockley-

Read-Hall rate and the Auger coefficient to be  $2.4 \times 10^8 \text{ s}^{-1}$  and  $7 \times 10^{-27} \text{ cm}^6/\text{s}$ , respectively.

The source that is most influential and cited the most in this thesis is the dissertation by Cooley (1997). He investigated the radiative and nonradiative recombination coefficients of three InAsSb MQW lasers as a function of well and barrier thickness and temperature. His setup consisted of a mode-locked Ti:Sapphire laser which produced 200 fs pulses. His results can best be summed up with Table 3.1 below.

Laser Sample	Temp (K)	QW/Barrier Thickness (nm/nm)	Number of Wells ( $t_{\text{qw}}$ )	$\tau_{\text{SRH}}$ (ns)	$B_{\text{rad}}$ ( $\text{cm}^3/\text{s}$ )	$C_{\text{Auger}}$ ( $\text{cm}^6/\text{s}$ )
A	77	15/30	10	12	$2.0 \times 10^{-10}$	$< 1 \times 10^{-29}$
B	77	10/20	10	10	$2.0 \times 10^{-10}$	$< 1 \times 10^{-29}$
B	150	10/20	10	1.7	$0.78 \times 10^{-10}$	$7.0 \times 10^{-28}$

Table 3.1: Radiative and nonradiative coefficients for sample A and B at 77 and 150 K after Cooley (1997).

Cooley also developed a novel method to analyze his data in order to extract the recombination coefficients from his data. This thesis will be partially adopting his method when analyzing the data. The details of this method and how it differs from Cooley's will be covered in Chapter 5.

In 1998, Jang *et al.* performed TRPL on an AlGaInAsSb/InAs/GaInSb broken-gap superlattice to determine the Auger recombination coefficient at temperatures ranging from 50 to 300 K. They reported the Auger coefficient to be  $2.9 \times 10^{-27} \text{ cm}^6/\text{s}$  at 300 K. However, they did not determine the SRH or radiative recombination coefficients.

Finally, in 1999, Flatté *et al.* reported on recombination rates in narrow-gap InAs/Ga<sub>1-x</sub>In<sub>x</sub>Sb-based superlattices. They performed time-resolved differential transmission and time-resolved photoluminescence, and determined that the Auger

recombination rate depended on carrier density as  $n^2$  for low density, and changed to an  $n$  dependence when the electrons and holes became degenerate. They, too, did not determine SRH or radiative recombination coefficients.

## **4.Experimental and Analytical Procedures, and Samples**

This chapter will cover the specifics of the experimental setup that were used to perform TRPL, the analytical procedure, and the samples studied. First, this chapter will begin with an overview of the components in the setup. Second, the basic theory involved in predicting crystal tilt for both KTA and LiIO<sub>3</sub> non-linear crystals and exit angle for either the sum frequency generated (SFG) or second harmonic generated (SHG) beam will be discussed. This will lead to the importance to finding zero path length and of how time-resolved photoluminescence can be accomplished. Next, a detail description of the analytical procedure, and how it differs from the one Cooley (1997) used, will be discussed. And finally, the chapter will close with a composition of the samples studied.

### **4.1. The Setup**

The setup (Figure 4.1) begins with an argon-ion (Ar<sup>+</sup>) laser that pumps a Coherent Mira 900, mode-locked, Ti:Sapphire laser operating at 800 nm with an output power of approximately 1.4 Watts. The Ti:Sapphire laser employs an ingenious yet simple method that passively mode-locks the output of the laser. Mode-lock refers to the output of the laser being pulsed, not continuous.

The pulses exiting the laser have a repetition rate of 76 MHz and a pulse width of 120 fs. The pulse width was measured using an INRAD Model 5-14BX Autocorrelator. Figure 4.2 shows a typical autocorrelation trace of a Ti:Sapphire pulse. Assuming that the pulse shape takes the form of a hyperbolic secant function, the ratio of actual pulse width to the autocorrelation pulse width is 0.684. The autocorrelation measured a pulse width of 0.172 ps, which corresponds to an actual pulse width of 118 fs.

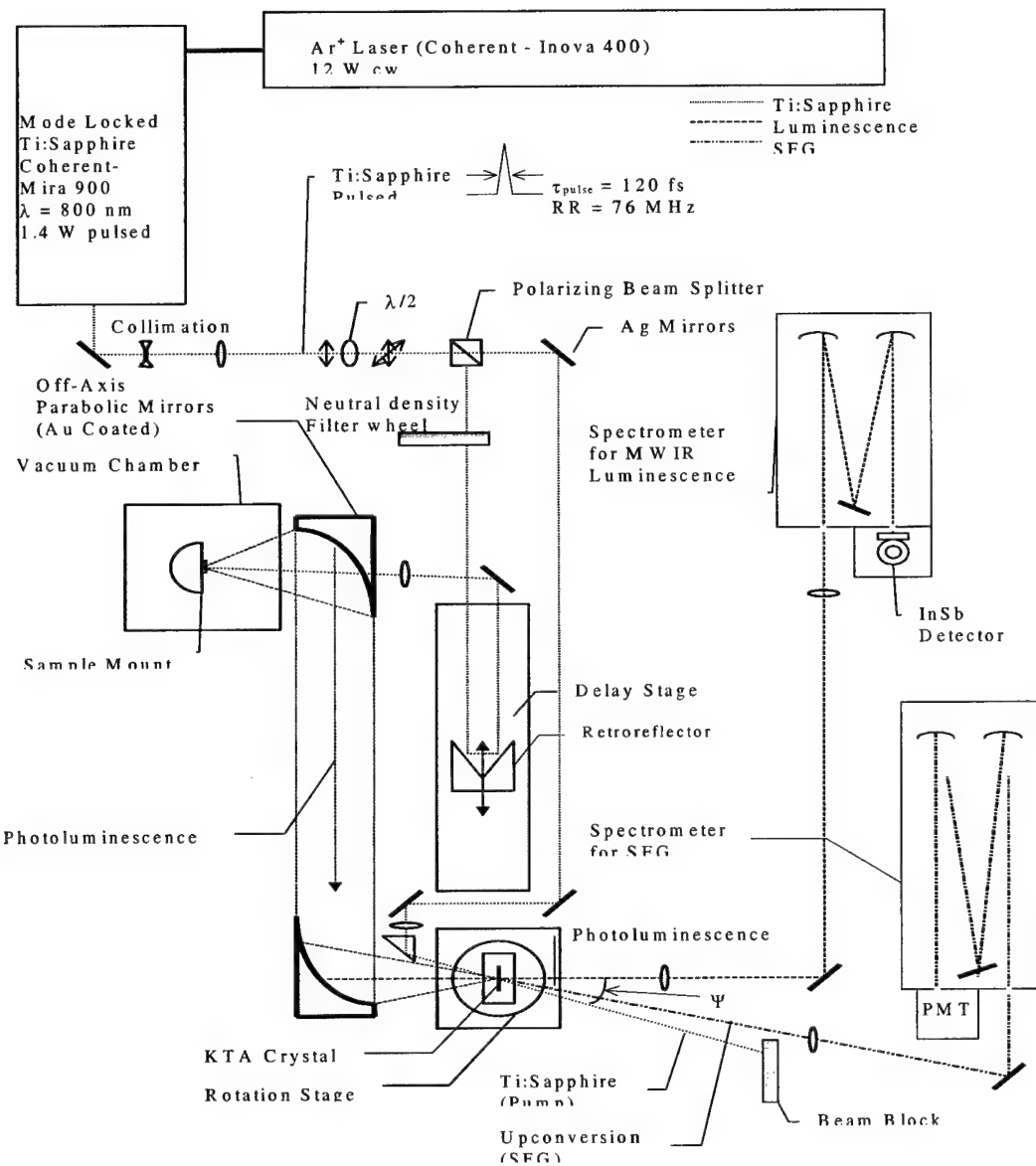


Figure 4-1: Experimental setup of the upconversion experiment after Cooley (1997).

As the beam exits the Ti:Sapphire laser, it is expanded and collimated using a set of lenses. The beam is then sent through a long-pass filter ( $\lambda > 700$  nm) in order to filter out the spontaneous emission of photons from the highly excited Ti:Sapphire crystal. Afterward, the beam travels through a  $\lambda/2$  wave plate before encountering a polarizing beam splitter. The

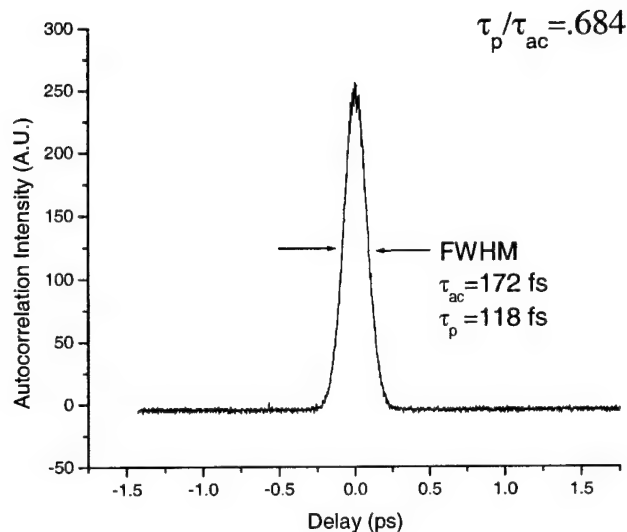


Figure 4-2: Autocorrelation of mode-locked Ti:Sapphire laser.

polarizing beam splitter splits the beam into two legs: the PL leg and pump leg. By adjusting the  $\lambda/2$  wave plate, in conjunction with the beam splitter, one can control the amount of laser power that goes into each leg. The PL leg refers to the path, starting at the beam splitter, that the first part of the Ti:Sapphire beam takes to reach the sample, and the path that the luminescence takes to reach the rotation stage. Beginning at the beam splitter, the beam goes through a neutral density filter wheel and reflects off of a gold-coated retroreflector, which is mounted on a delay stage, before being focused onto the sample being investigated. The neutral density filter allows one to adjust the amount of laser power that excites the sample independent from the pump leg. The delay stage gives one the ability to increase or decrease the optical path length of the PL leg. The laser beam excites the sample and causes the sample to luminesce. The luminescence is collected and collimated with an off-axis parabolic mirror. The parabolic mirror sends the collimated luminescence to a second off-axis parabolic mirror where it is focused at the center of rotation of the rotation stage.

The sample is mounted on a cold finger inside a vacuum chamber, which has a base pressure of  $5.0 \times 10^{-5}$  Torr. This is done to prevent condensation from forming on the sample during the experiments. The exit window of the chamber is made of LiF, which transmits very well in the mid-infrared. The faces of the LiF window were not perfectly flat and were believed to have a lensing effect on the luminescence. This effect would lead to an aberrated focus at the rotation stage. To minimize the lensing affect, an extension was designed and fabricated to place the sample closer to the window. By doing so, the cone of luminescence transmits through a smaller portion of the window and lensing is minimized.

When conducting photoluminescence experiments, the luminescence is collected and collimated using a CaF<sub>2</sub> lens and sent to another CaF<sub>2</sub> lens before being focused into the slits of a 0.5 meter McPherson grating spectrometer, which is equipped with a liquid-nitrogen-cooled InSb detector. CaF<sub>2</sub> lenses are used since they transmit well in the mid-infrared.

The pump leg refers to the path taken by the second part of the Ti:Sapphire beam, which is referred to as the pump beam. Again, starting at the beam splitter, the pump beam is guided by five mirrors to a lens before being focused at the center of rotation of the rotation stage. The angle between the PL beam and the pump beam at the rotation stage is 20°.

When conducting SFG or upconversion experiments, the pump beam and the luminescence overlap in time and space within a nonlinear crystal in order to produce a third, upconverted photon. This technique will be discussed in detail in the next section. The upconverted photons are detected with a 0.75-meter Spex grating monochromator. The Spex used a GaAs photomultiplier tube (PMT) detector biased at 2000 V and operated at 0 °C. When collecting the upconverted photons, there are two setups that can be used: a one-lens system or a two-lens system.

The one-lens system consists of one lens with a 400-cm focal length positioned such that upconverted photons generated at the center of rotation of the rotation stage are imaged onto the slits of the spectrometer. The advantage to the one-lens system is that the pump beam is not collected by the lens and, therefore, the overall noise is minimized. The disadvantage is the system is aligned for only one wavelength of upconverted photons and, if a different luminescent wavelength is desired to be upconverted, the one lens system must be realigned.

The two-lens system consists of two lenses in which one lens, with focal length approximately 10 cm, is placed a focal length away from the center of rotation of the rotation stage. The upconverted photons are then collected and collimated to the second lens before being focused onto the slits of the monochrometer. The advantages to the two-lens system are that all wavelengths of upconverted photons are collected simultaneously and the setup does not need to be realigned if different luminescent wavelengths are desired to be upconverted. The disadvantage is that the pump beam is collected, as well, and sent directly into the monochrometer. Much filtering of the upconverted photons is needed, which also filters out some of the photons of interest.

The one-lens system was chosen for this experiment.

Procedures for aligning this experiment are detailed in Appendix B.

#### **4.2. Upconversion Technique**

The upconversion technique involves the mixing of two photons of different wavelengths within a nonlinear crystal, which results in the production of a third photon having a wavelength different from the other two. However, the two photons must overlap in time and space in order for upconversion to take place. Details of the nonlinear process of upconversion are beyond the

scope of this thesis, but results can be easily predicted with two simple concepts, conservation of momentum and conservation of energy. Conservation of energy allows for the prediction of the upconverted wavelength ( $\lambda_{\text{up}}$ ) given the wavelength of the photoluminescence ( $\lambda_{\text{PL}}$ ) and the wavelength of the pump beam ( $\lambda_{\text{pump}}$ ).

$$1/\lambda_{\text{up}} = 1/\lambda_{\text{PL}} + 1/\lambda_{\text{pump}} \quad (4-1)$$

Conservation of momentum allows for the prediction of angle tilt of the crystal as well as the exit angle of the upconverted photons. Figure 4.3 shows a graphical representation of momentum conservation within the crystal where the symbol ( $\vec{k}$ ) represents the momentum vector of a photon. The momentum vector of a photon is related to the wavelength of that photon and the index of refraction (n) of the material that the photon is propagating in by Equation 5-2.

$$\vec{k} = \frac{2\pi n}{\lambda} \quad (4-2)$$

A Mathematica program was developed to predict the upconverted wavelength, the angle tilt of the crystal, and exit angle of the upconverted photons given the index ellipsoid for the crystal, the PL wavelength, the pump wavelength, and the angle between the two, relative to the crystal. These Mathematica files are presented in Appendix B.

### 4.3 Zero Path Length

One of the most important aspects of this experiment is determining zero path length. Zero path length is defined as the position of the delay stage that makes the optical length of both PL and pump leg equal. It is crucial to know this particular position of the delay stage because it is at this position where the pump pulse arrives at the center of rotation of the rotation stage at the same time that the leading edge of the photoluminescence pulse does. Determining zero path

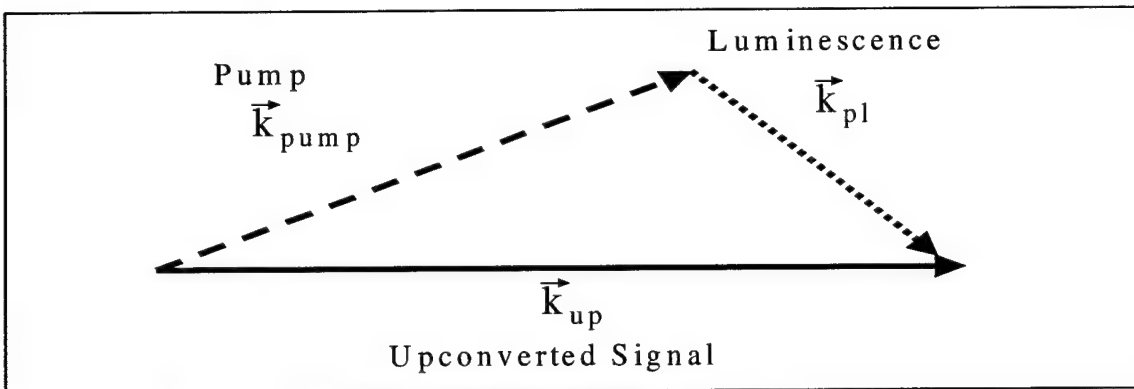


Figure 4-3: Graphical representation of momentum conservation within nonlinear crystal.

length is accomplished using SHG, which is a special case of SFG in which the photons being mixed inside the crystal have the same wavelength. The crystal used here for SHG was LiIO<sub>3</sub>. This particular crystal was cut at 39° with respect to the x-axis of the crystal. The crystal is mounted such that its center is at the center of rotation of the rotation stage. Beams that travel down both legs in the experiment overlap in space within the crystal. The PL beam is focused down to a spot size of about 25 μm, while the pump beam is focused down to a spot size of about 35 μm. The spot sizes were measured using the knife-edge method by Cooley (1997) and, since the optics have not changed, the spot sizes are assumed not to have either. A 100-μm-diameter pinhole was used to overlap both beams at the center of rotation of the rotation stage. In SHG, the Ti:Sapphire is mixed with itself inside the LiIO<sub>3</sub> crystal. This is accomplished by allowing the Ti:Sapphire beam to scatter off the cold finger instead of exciting the sample. Therefore, the scatter of the Ti:Sapphire is collected by the parabolic mirror rather than the luminescence of the sample. According to the Mathematica program, the crystal should be tilted to approximately

$20^\circ$  with respect to the PL beam and the SHG photons, of wavelength 400 nm, which is a dark purple, should exit the crystal at  $10^\circ$  with respect to the table.

Recall that the Ti:Sapphire and therefore the scatter of the Ti:Sapphire are pulsed. With the two beams overlapping in space within the crystal, they now have to overlap in time in order to produce the SHG photons. This is done by moving the delay stage until a purple beam can be observed. The SHG beam is typically intense enough to be observed with the naked eye. When this beam is observed, the position of the delay stage is set to zero ps delay.

#### 4.4 Time-Resolved Photoluminescence

Having found zero path length, the Ti:Sapphire is repositioned so that it excites the sample being investigated. When performing TRPL, the same alignment procedure used in finding zero path length is employed excepted that the  $\text{LiIO}_3$  crystal is replaced with a  $\text{KTiOAsO}_4$  (KTA) crystal. For a given Ti:Sapphire pulse that excites the sample, the luminescence given off by the sample is also pulsed and exhibits the form depicted in Figure 4.4. Figure 4.4a shows the exciting pulse, at zero path length, and the resulting luminescence decay over time which is typically on the order of less than 5 ns. Figure 4.4b shows how the pump pulse is mixed with different parts of the luminescence by means of the delay stage. By moving the delay stage, the pump pulse can mix with portions of the luminescence, in time, within the crystal. Since the number of upconverted photons is directly proportional to the intensity of the luminescence, the upconverted signal directly maps out the decay of the luminescence.

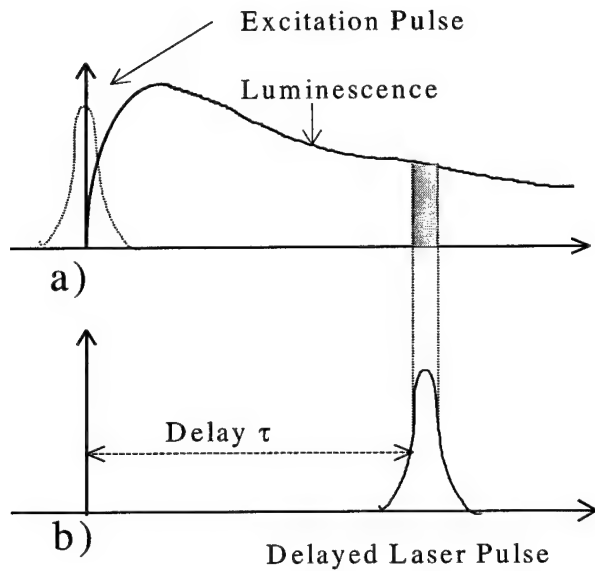


Figure 4-4: Excitation pulse and luminescence decay as a function of time (a). Delayed laser pulse  $\tau$  ps away from zero path length(b).

#### 4.5 Analytical Procedure

The analysis begins with the differential recombination rate equation

$$-\frac{dn}{dt} = A_{SRH}n + B_{rad}n^2 + C_{Auger}n^3, \quad (4-3)$$

which assumes an intrinsic material. Solving this differential equation with Mathematica results in an analytical solution of the form

$$t(n) = \frac{-1}{2A} \text{Ln} \left[ \frac{n^2}{A + Bn + Cn^2} \right] + \frac{B}{A\sqrt{4AC - B^2}} \arctan \left[ \frac{2Cn + B}{\sqrt{4AC - B^2}} \right]. \quad (4-4)$$

Notice that Equation 4-4 represents time,  $t$ , as a function of carrier density,  $n$ , and the recombination coefficients. However, the TRPL experiment results in data in the form of upconversion signal as a function of time,  $L(t)$ . The first obstacle is to convert from

upconversion signal, L(t), to a carrier density, n(t). This is achieved by applying the initial carrier density equation

$$n(t_0) = \left( \frac{P/RR}{h\nu} \right) \left( \frac{1}{N_{qw}\pi w_{PL}^2} \cdot \frac{t_{InAs} + t_{GaInSb}}{t_{InAs} \cdot t_{GaInSb}} \right) (1-R) [1 - \exp(-\alpha \cdot N_{qw}(t_{InAs} + t_{GaInSb}))] \left( \frac{1}{1 + \frac{w_p^2}{w_{PL}^2}} \right) \quad (4-5)$$

which was adapted from Cooley (1997). The first term represents the number of photons per pulse, where P is the power of the Ti:Sapphire laser that was used to excite the sample, RR is the repetition rate of the laser, and  $h\nu$  is the energy of each photon. The second term represents the number of carriers per unit volume, where  $N_{qw}$  is the number of quantum wells,  $w_{PL}$  is the spot size of the laser on the sample, and  $t_{InAs}$  and  $t_{GaInSb}$  are the thicknesses of the InAs and GaInSb layers, respectively. The third term represents the fraction of light that is transmitted through the surface of the sample, where R is the power reflectance at the surface of the samples. R can be determined using the equation

$$R = \left( \frac{n_s - 1}{n_s + 1} \right)^2, \quad (4-6)$$

where  $n_s$  is the index of refraction for the surface material of the sample. The index of refraction for these samples was chosen to be 4.39 after Madelung (1991). The fourth term represents the fraction of light that is absorbed by the quantum wells where  $\alpha$  is the absorption coefficient. Cooley (1997) measured  $\alpha$  via ellipsometry. However, due to time constraints, ellipsometry could not be performed on the samples studied in this work so an educated guess had to be made as to the value of  $\alpha$ . The value chosen was  $2.5 \times 10^5 \text{ cm}^{-1}$  since it is within an order of magnitude

from the  $\alpha$  measured by Cooley. The last term represents the overlap efficiency of the PL and pump beams inside the nonlinear crystal, where  $w_p$  is the spot size of the pump beam at the crystal.

For a given sample, Equation 4-5 can be used to find the initial carrier density for a particular pump power, which is only valid at time  $t_0$ . Since there is a corresponding upconversion signal for each pump power at  $t_0$ , one can create an empirical relationship between upconversion signal and carrier density,  $n(L)$ . Once  $n(L)$  is known, it can easily be fitted to a function such that the conversion between carrier density and upconversion signal can be made at times greater than  $t_0$ . The fitting function used was

$$n(L) = u_0 L + u_1 L^{u_2}, \quad (4-7)$$

where  $u_0$ ,  $u_1$ , and  $u_2$  are fitting parameters.

#### 4.5.1 Curve Fitting

Using the empirical relation  $n(L)$ , the raw upconversion data can be converted from  $L(t)$  to  $n(t)$ . However, recall that the solution to Equation 4-4 is of the form  $t(n)$ . Here is where the method of analyzing the data of this thesis diverges from that of Cooley (1997). Cooley numerically inverted Equation 4-4 in order to directly apply it to his data. Once inverted, he manually selected recombination coefficients that best fit his data visually. The approach taken in this thesis was to graphically invert the converted data so that Equation 4-4 could be directly fit using Microcal's Origin software package. The advantages of this method were that it is straight forward, faster, and that the curve fits are determined via Least-Squares method rather than visually.

## **4.Experimental and Analytical Procedures, and Samples**

This chapter will cover the specifics of the experimental setup that were used to perform TRPL, the analytical procedure, and the samples studied. First, this chapter will begin with an overview of the components in the setup. Second, the basic theory involved in predicting crystal tilt for both KTA and LiIO<sub>3</sub> non-linear crystals and exit angle for either the sum frequency generated (SFG) or second harmonic generated (SHG) beam will be discussed. This will lead to the importance to finding zero path length and of how time-resolved photoluminescence can be accomplished. Next, a detail description of the analytical procedure, and how it differs from the one Cooley (1997) used, will be discussed. And finally, the chapter will close with a composition of the samples studied.

### **4.1. The Setup**

The setup (Figure 4.1) begins with an argon-ion (Ar<sup>+</sup>) laser that pumps a Coherent Mira 900, mode-locked, Ti:Sapphire laser operating at 800 nm with an output power of approximately 1.4 Watts. The Ti:Sapphire laser employs an ingenious yet simple method that passively mode-locks the output of the laser. Mode-lock refers to the output of the laser being pulsed, not continuous.

The pulses exiting the laser have a repetition rate of 76 MHz and a pulse width of 120 fs. The pulse width was measured using an INRAD Model 5-14BX Autocorrelator. Figure 4.2 shows a typical autocorrelation trace of a Ti:Sapphire pulse. Assuming that the pulse shape takes the form of a hyperbolic secant function, the ratio of actual pulse width to the autocorrelation pulse width is 0.684. The autocorrelation measured a pulse width of 0.172 ps, which corresponds to an actual pulse width of 118 fs.

## **5. Results and Analysis**

This chapter will cover the results obtained for the TRPL experiment. The first section will present the photoluminescence results for both samples. The second section will present the raw TRPL data for samples 90 and 91 at 77 K and 5.5 K. The third section, using the analytical procedure discussed in Chapter 4, will present the individual curve fitted data and the fourth section will present the representative coefficients for both samples at both temperatures.

### **5.1 Photoluminescence Results**

Photoluminescence experiments were first performed on the samples to determine the peak wavelength of the luminescence curves. It is the peak wavelength that is investigated in the TRPL experiments. Figure 5-1 shows the results of the photoluminescence experiments for both samples at 77 K and 5.5 K temperatures. Notice that sample 91 is brighter than sample 90, as well as the red shift in wavelength from sample 91 to 90. This red shift is accounted for by the lowering of the bound energy states in a quantum well as the width of the well is increased. Once the peak wavelength of the luminescence is known, TRPL experiments can be performed.

### **5.2 TRPL Data**

Recall that TRPL involves the mixing of a PL and pump beam within a nonlinear crystal resulting in the production of a third, upconverted beam. This technique allows one to map out the luminescent decay of a single wavelength as a function of time. The

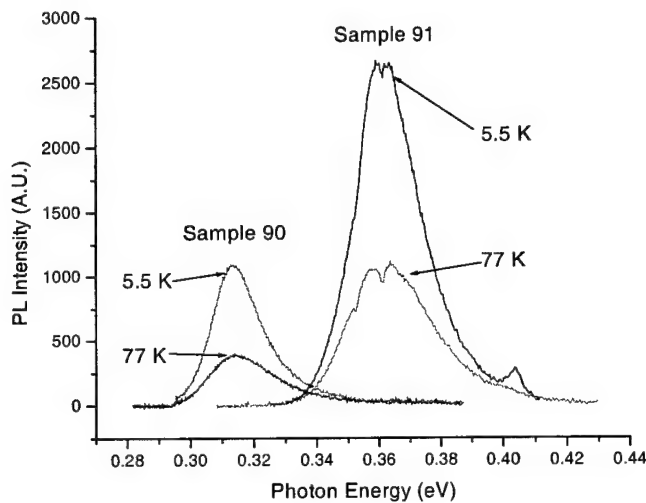


Figure 5-1: Photoluminescence of samples 90 and 91 at 77 K and 5.5 K.

selection of the individual wavelengths to be upconverted is determined by the tilt of the crystal. When investigating sample 90, which has a luminescence peak at 3.95  $\mu\text{m}$ , the KTA crystal was tilted to 22.3° with respect to the table. When investigating sample 91, which has a luminescence peak at 3.45  $\mu\text{m}$ , the KTA crystal was tilted to 19.1° with respect the table.

Figures 5-2 through 5-5 show the TRPL results for samples 90 and 91 at 77 K and 5.5 K. The luminescent decay is a result of the depletion of the carrier density in the higher energy state over time. Recall that sample 91 was brighter than sample 90. The data reflects this as a larger peak PMT signal, or upconversion signal, for sample 91 compared to that of sample 90 at a given temperature. The faster rate of decay of the upconversion signal for sample 90 compared to that of sample 91, at a given temperature, is also indicative of sample 91 being the brighter sample.

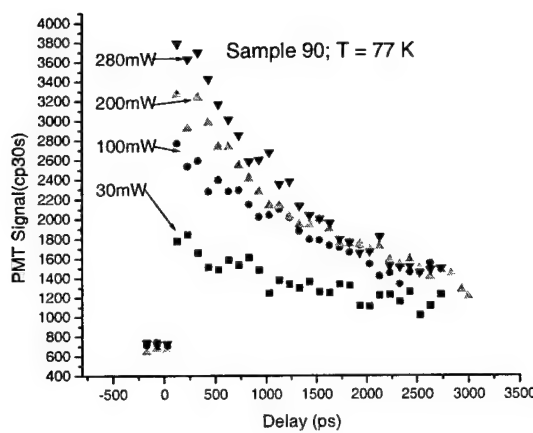


Figure 5-2: Raw upconversion data for sample 90 at 77 K.

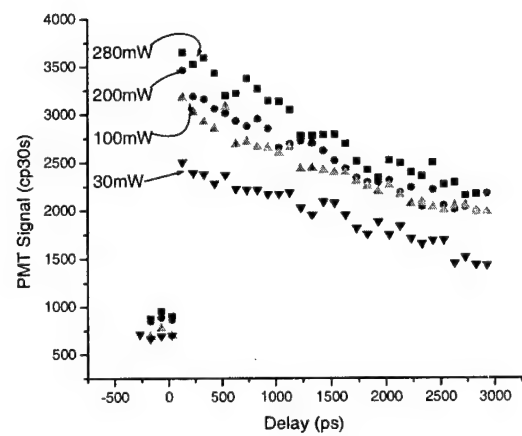


Figure 5-3: Raw upconversion data for sample 90 at 5.5 K

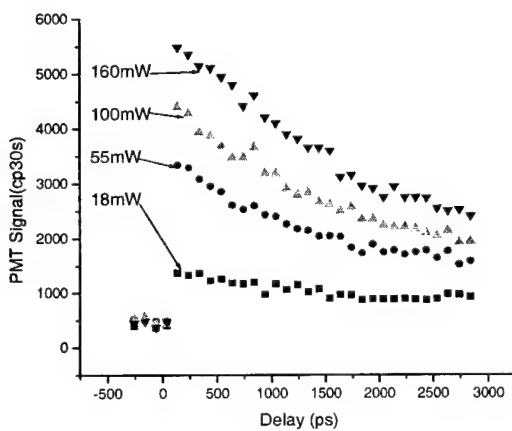


Figure 5-4: Raw upconversion data for sample 91 at 77 K.

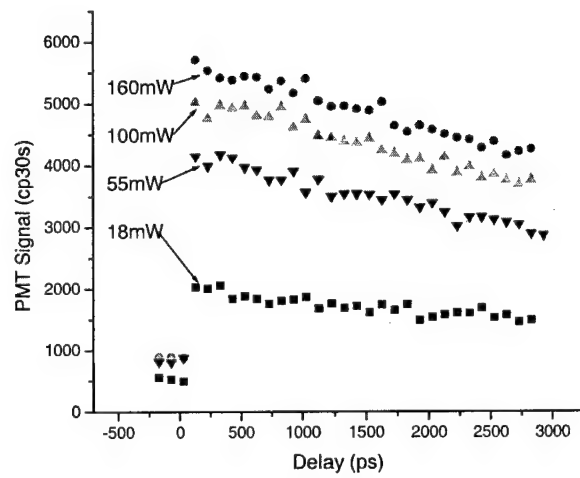


Figure 5-5: Raw upconversion data for sample 91 at 5.5 K.

### 5.3 Individual Curve Fitted TRPL Data

The raw TRPL data,  $L(t)$ , was converted to  $n(t)$  via the empirical relation,  $n(L)$ , presented in Chapter 4, then graphically inverted. Figure 5-6 shows the curve fits for  $n(L)$  for both samples at both temperatures. Each curve from each set was curve fitted in order to obtain the recombination coefficients. The results of the individual curve fits are shown in Figure 5-7 through Figure 5-10. Tables 5-1 through 5-4 give the coefficients for each curve for a given set. The curve fits for each set visually fit very well. However, in order to get the curves to fit well, different coefficients for each curve were used, when in fact, there should only be a single set of coefficients for each sample at each temperature. The method of determining these single sets of coefficients for each sample at each temperature is discussed in the next section.

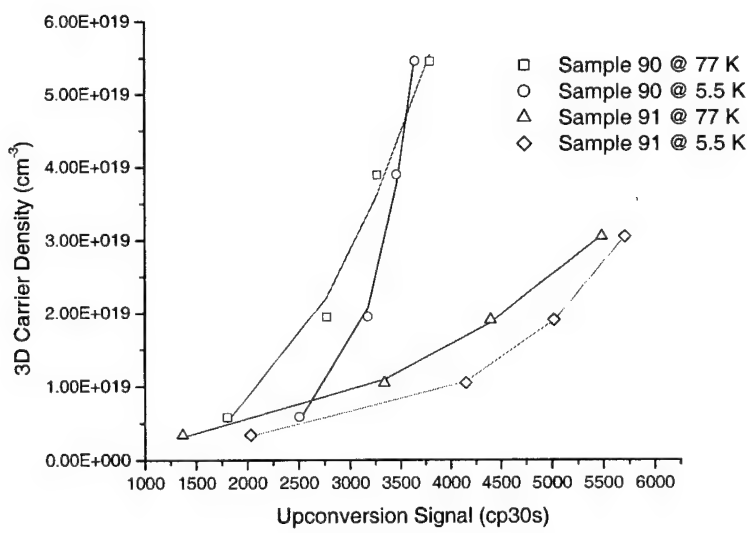


Figure 5-6: Conversion from upconversion to carrier density for samples 90 and 91 at 77 K and 5.5 K

### **5.3.1 Individual Curve Fits for Sample 90**

At 77 K, all three coefficients increase as the pump power increases. This trend may not be very significant but may give some insight into why the single set of coefficients do not fit the data well in the next section.

One expects the Auger coefficient to be smaller at lower temperatures than at higher temperatures. This can be seen when comparing the Auger coefficients, collectively, for sample 90 at 77 K and 5.5 K. The radiative coefficients, collectively, seem to be higher at 77 K than at 5.5 K. These trends explain why this sample is brighter at 5.5 K than at 77 K. It is difficult to say anything about the SRH coefficients for either temperature since the coefficients vary so much at 5.5 K.

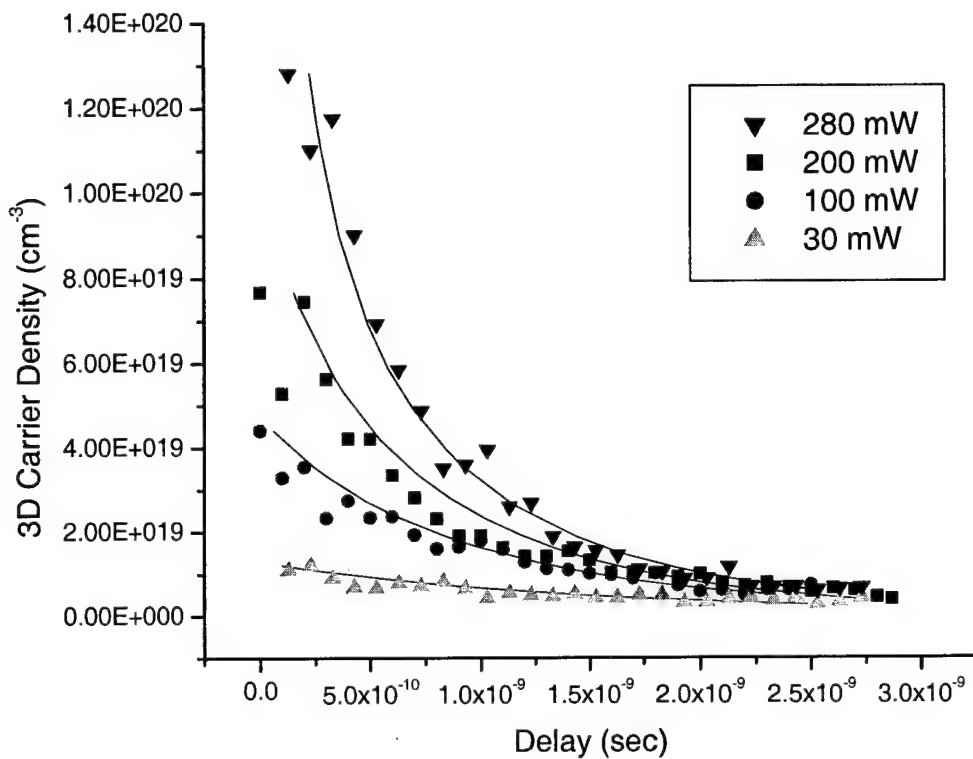


Figure 5-7: Best individual curve fits for sample 90 at 77 K.

Pump Power	$A_{SRH}^{-1}$ (ns)	$B_{rad}$ (cm <sup>3</sup> /sec)	$C_{Auger}$ (cm <sup>6</sup> /sec)
30 mW	1.64	5.55E-12	1.48E-32
100 mW	1.22	8.25E-12	2.48E-32
200 mW	1.04	8.55E-12	2.98E-32
280 mW	1.04	8.55E-12	6.54E-32

Table 5-1: Individual coefficients for sample 90 at 77 K.

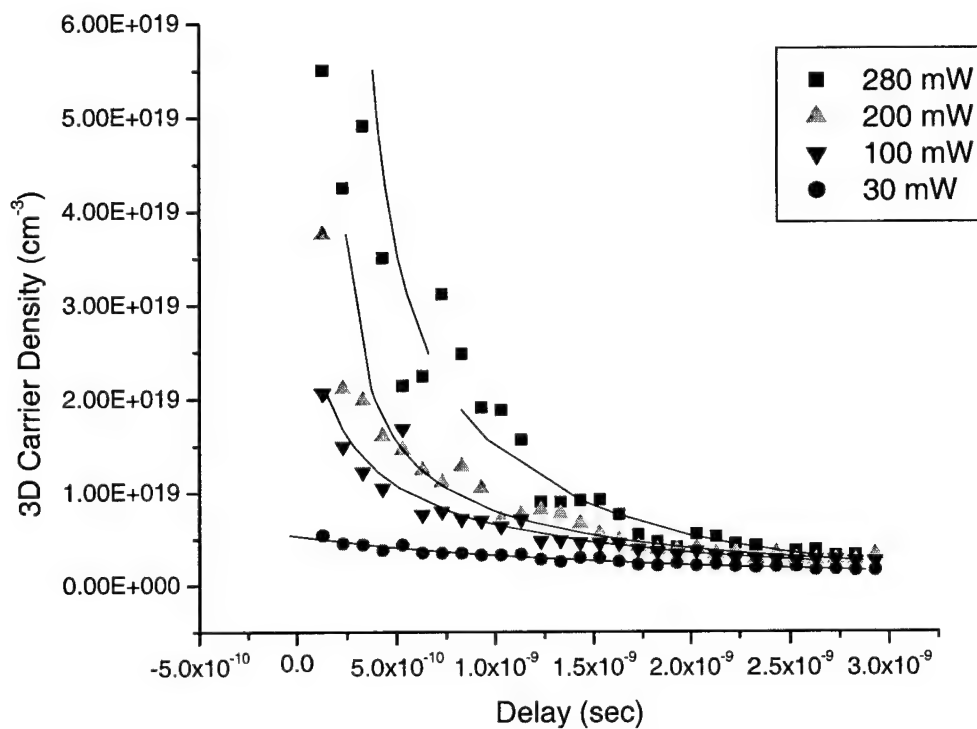


Figure 5-8: Best individual curve fits for sample 90 at 5.5 K.

Pump Power	$A_{SRH}^{-1}$ (ns)	$B_{rad}$ (cm <sup>3</sup> /sec)	$C_{Auger}$ (cm <sup>6</sup> /sec)
30 mW	4.18	4.58E-11	3.54E-30
100 mW	3.97	5.74E-11	3.54E-30
200 mW	3.97	5.74E-11	3.54E-30
280 mW	1.37	2.04E-11	1.04E-30

Table 5-2: Individual coefficients for sample 90 at 5.5 K.

### 5.3.2 Individual Curve fits for Sample 91

The SRH and radiative coefficients for all pump powers at both temperatures do not vary very much, if at all. The Auger coefficient is the only one that changes for different pump powers at both temperatures. This coefficient also seems to increase as the pump power increases for both temperatures.

Collectively, the Auger coefficient is larger at 77 K than at 5.5 K, which could explain why sample 91 is brighter at the lower of the two temperatures.

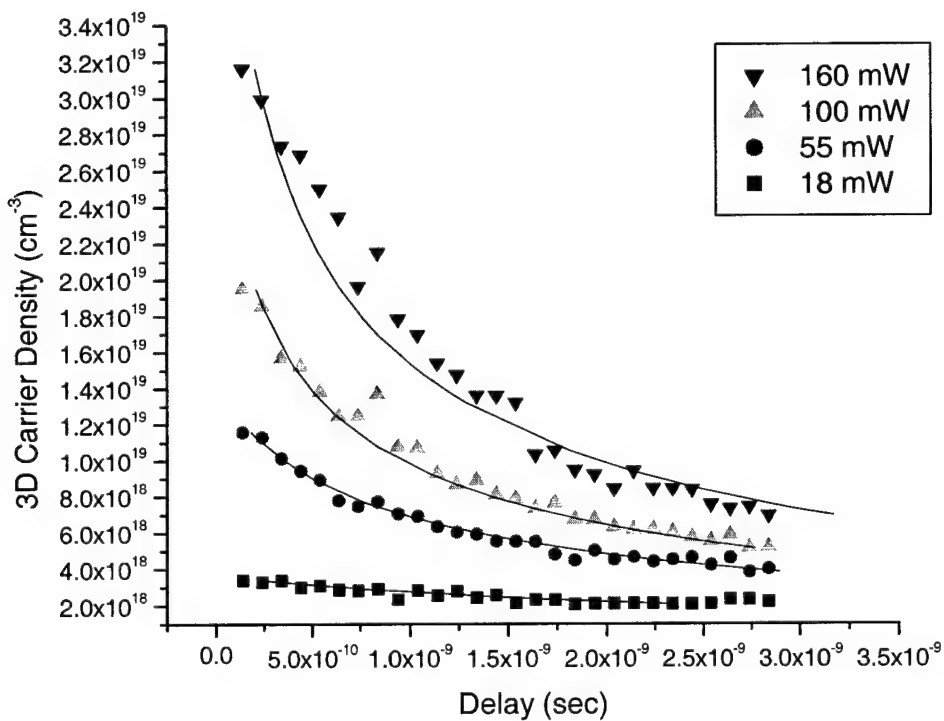


Figure 5-9: Best individual curve fits for sample 91 at 77 K.

Pump Power	$A_{SRH}^{-1}$ (ns)	$B_{rad}$ ( $\text{cm}^3/\text{sec}$ )	$C_{Auger}$ ( $\text{cm}^6/\text{sec}$ )
18 mW	11	1.62E-11	1.45E-29
55 mW	11	1.73E-11	5.03E-29
100 mW	10	1.73E-11	2.95E-29
160 mW	10.9	1.71E-11	9.69E-29

Table 5-3: Individual coefficients for sample 91 at 77 K.

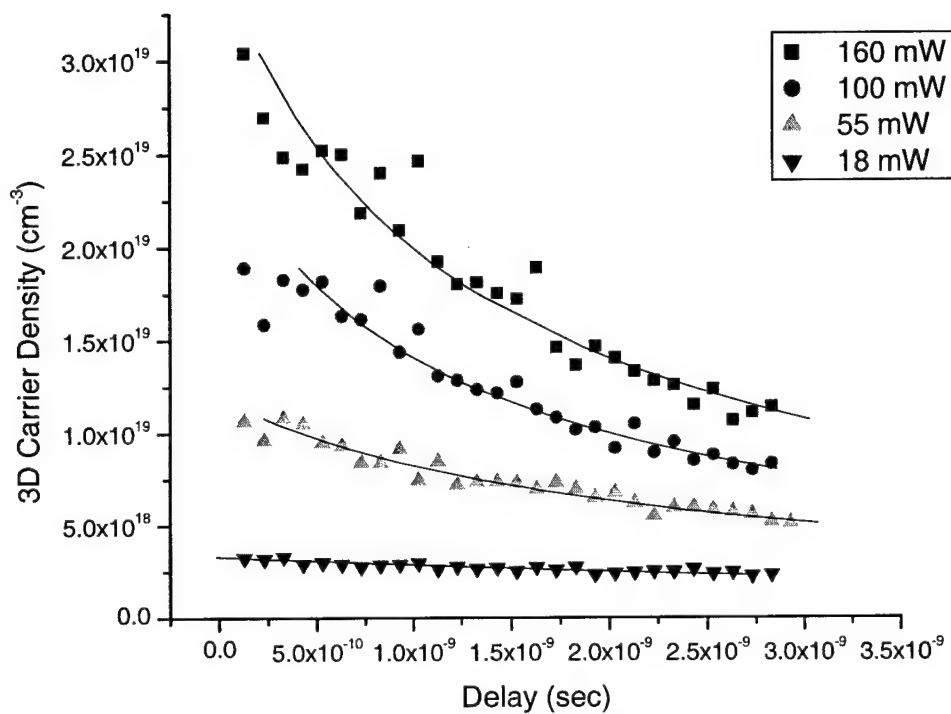


Figure 5-10: Best individual curve fits for sample 91 at 5.5 K.

Pump Power	$A_{SRH}^{-1}$ (ns)	$B_{rad}$ (cm <sup>3</sup> /sec)	$C_{Auger}$ (cm <sup>6</sup> /sec)
18 mW	10.8	1.02E-11	1.82E-30
55 mW	10.8	1.03E-11	1.81E-30
100 mW	10.8	1.03E-11	9.09E-31
160 mW	10.8	1.03E-11	3.09E-31

Table 5-4: Individual coefficients for sample 91 at 5.5 K.

## 5.4 Representative Recombination Coefficients

Once the coefficients from a given set are obtained, they are used to help to determine a single set of coefficients that represents all curves in a single set. Using these representative coefficients, the data from each set is refitted to determine how well those coefficients represent that set. Figures 5-11 through 5-14 show the results of the final curve fits with the representative recombination coefficients.

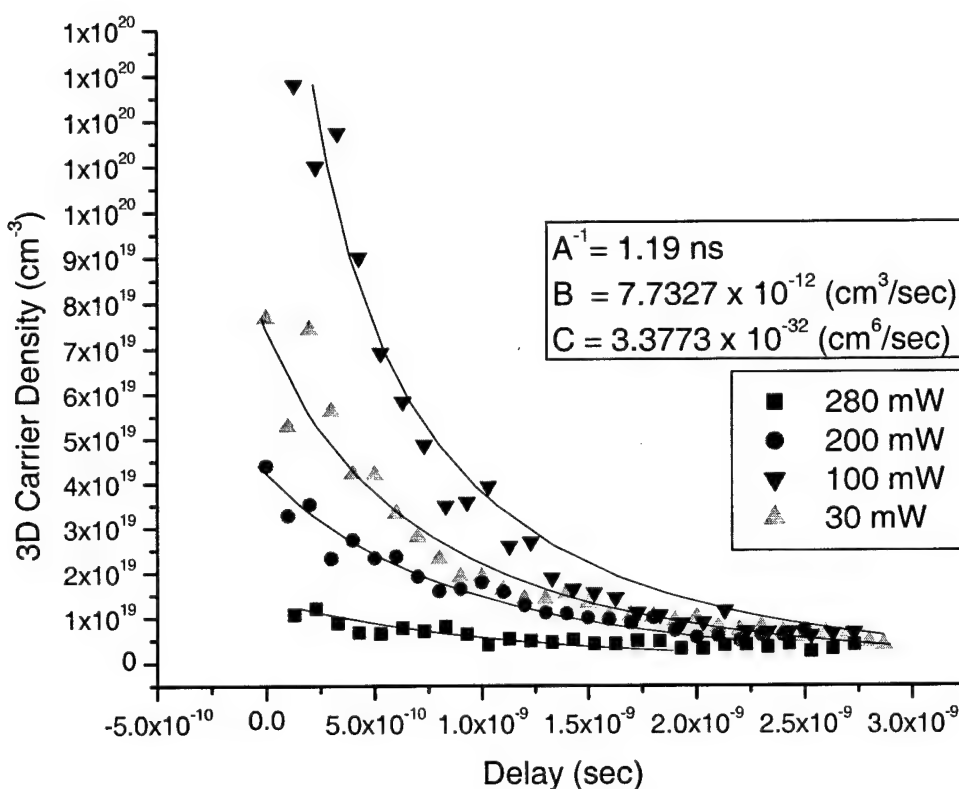


Figure 5-11: Curve fits with representative coefficients for sample 90 at 77 K.

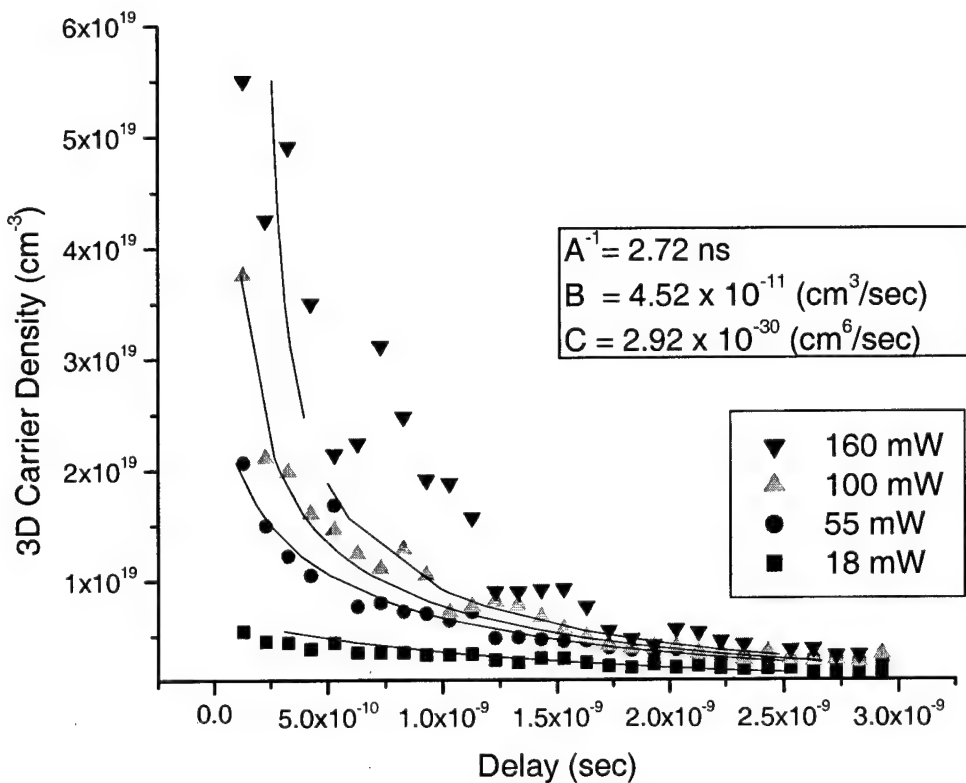


Figure 5-12: Curve fits with representative coefficients for sample 90 at 5.5 K.

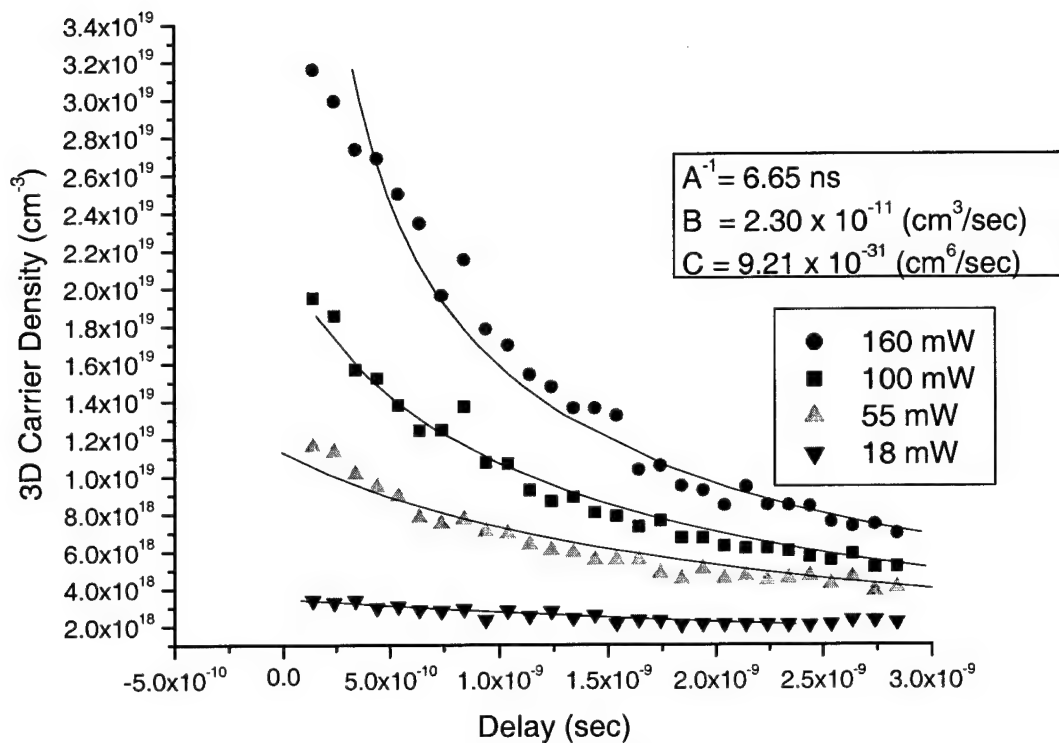


Figure 5-13: Curve fits with representative coefficients for sample 91 at 77 K.

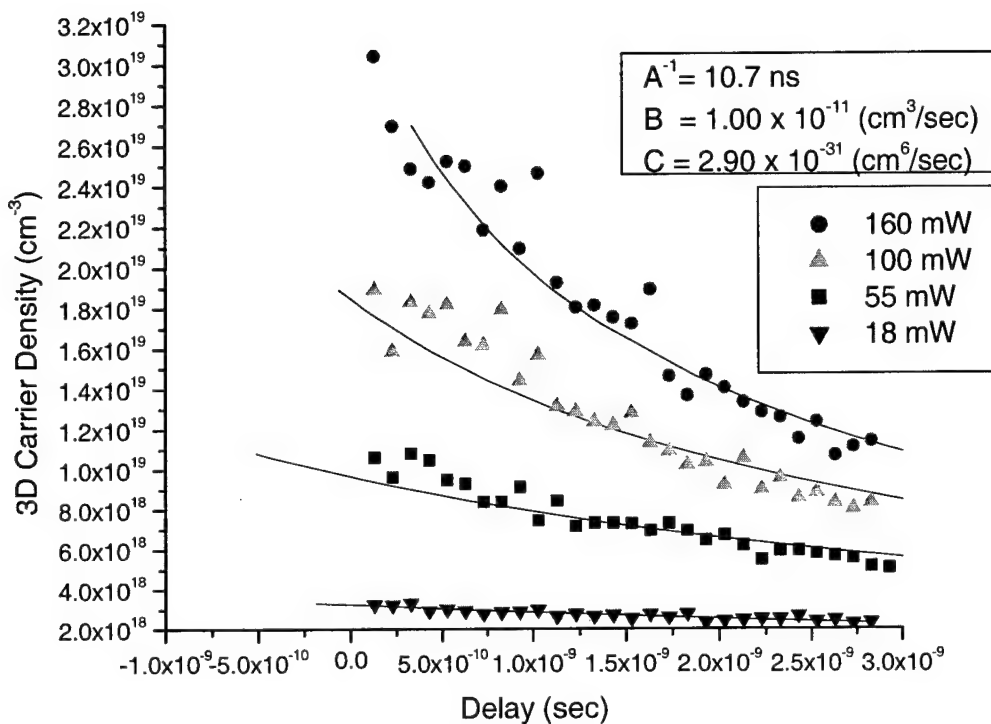


Figure 5-14: Curve fits with representative coefficients for sample 91 at 5.5 K.

## 5.5 Summary

The final set of recombination coefficients for samples 90 and 91 at 77 K and 5.5 K are given in Table 5-5. The curve fits using the coefficients from Table 5-5, i.e. Figures 5-11 through 5-14, fit well. As mentioned before, sample 91 was brighter than sample 90. One would expect the radiative coefficient for sample 91 to be greater than that of sample 90. The radiative coefficient reflects this intuition, however, it would be

difficult to say the brightness of the samples is dictated by this coefficient since they are so close to each other. If the radiative coefficient cannot give any insight, that leaves the non-radiative coefficients. Again, one would expect the Auger coefficient to be lower for the brighter sample. This is not the case. In fact, sample 91, the brighter of the two samples, has a greater Auger coefficient than sample 90. The only coefficient that follows one's intuition is the SRH lifetime ( $A_{SRH}^{-1}$ ). A longer lifetime indicates a lower SRH process. This would indicate that the SRH process is the dominant one and dictates the brightness of the samples.

The analysis above is based on the belief that the coefficients should differ from sample to sample by at least two orders of magnitude. Perhaps this belief is not entirely true. Maybe small differences in the coefficients result in large changes in the brightness of the samples and having a larger SRH lifetime and a larger radiative coefficient compounds this effect.

The validation of these coefficients comes from the comparison to the coefficients obtained by Cooley (1997). Cooley investigated Type I InAsSb quantum well laser structures and obtained recombination coefficients, Table 5-6, using TRPL. The coefficients from this thesis are within an order of magnitude of Cooley's. As mentioned before, Type I structures are believed to have a higher Auger coefficient than those of Type II structures. This can be seen by comparing the Auger coefficients from Table 5-5 and Table 5-6.

Sample	Temp (K)	$A_{SRH}^{-1}$ (ns)	$B_{rad}$ (cm <sup>3</sup> /sec)	$C_{Auger}$ (cm <sup>6</sup> /sec)
90	77	1.19	7.73E-12	3.37E-32
90	5.5	2.72	4.52E-11	2.91E-30
91	77	6.65	2.30E-11	9.21E-31
91	5.5	10.7	1.00E-11	2.90E-31

Table 5-5: Representative recombination coefficients for samples 90 and 91 at 77 K and 5.5 K.

Sample	Temp (K)	$A_{SRH}^{-1}$ (ns)	$B_{rad}$ (cm <sup>3</sup> /sec)	$C_{Auger}$ (cm <sup>6</sup> /sec)
Type I "B"	77	10	7.80E-11	7.00E-28

Table 5-6: Recombination coefficients obtained by Cooley (1997).

## 6. Conclusions and Future Work

The goal of this entire thesis was separated into two basic parts, the second being dependent on the first. The first, and most important, was to get the TRPL experiment running and capable of acquiring time-resolved data. As mentioned before, this experiment was inherited from Cooley (1997), but had been out of alignment and not operating at all for about three years. Once the experiment was operating correctly, it was used to acquire data on Type II InAs/GaInSb quantum well samples. The second part of this thesis was to analyze the data so that the recombination coefficients could be determined. A slightly different approach was taken when analyzing the data, compared to Cooley (1997), which proved to be more efficient. The final product of this thesis is presented in Table 6-1 below.

Sample	Temp (K)	$A_{SRH}^{-1}$ (ns)	$B_{rad}$ (cm <sup>3</sup> /sec)	$C_{Auger}$ (cm <sup>6</sup> /sec)
90	77	1.19	7.73E-12	3.37E-32
90	5.5	2.72	4.52E-11	2.91E-30
91	77	6.65	2.30E-11	9.21E-31
91	5.5	10.7	1.00E-11	2.90E-31

Table 6-1: Recombination coefficients for samples 90 and 91 at 77 K and 5.5 K.

### 6.1 Future Work

The validation of these coefficients comes mainly from the fact that they are near those obtained by Cooley. However, a thorough comparison cannot be made since the results from Cooley and this work were not analyzed using the same approach. An excellent follow up to this thesis would be to re-perform TRPL on Cooley's sample B at

5.5 and 77 K, perform TRPL on samples 90 and 91 and Cooley's sample B at 150 K, apply the analytical approach used in this work, and finally compare all the results.

Furthermore, the experimental setup could be improved. Installing larger off-axis parabolic mirrors would result in greater collection of the luminescence, which would increase the upconversion signal. Replacing the existing translation stage with a longer one would allow one to probe a greater portion of the luminescence decay.

## **Appendix A-Mathematica Files**

This appendix will present the Mathematica files used in determining crystal tilt and exit angle when performing both Sum Frequency Generation (SFG) and Second Harmonic Generation (SHG). The reader is expected to have some basic knowledge of the syntax of Mathematica.

### **A.1 Mathematic Files**

The foundation of these files is the index ellipsoids for both KTA and LiIO<sub>3</sub> crystals. The input for these files are the PL wavelength, in microns, and the pump wavelength, which is usually around 0.8 μm, and assumes an angle of 20° between the PL beam and the pump beam. There are two files for each crystal, one for when the crystal is right-side-up and one for when the crystal is up-side-down. This was done simply to see if it could be done. It also turns out that, when performing SHG, the SHG beam is much more clearer when the LiIO<sub>3</sub> crystal is up-side-down compared to when it is right-side-up. The files have been commented as much as possible and are presented below.

```
(*coe 2nd Harmonic Generation w/ LiIO3 Right Side Up*)

(*Index ellipsoid for LiIO3*)
nx[λ_] := Sqrt[3.415716 + 0.047031 / (λ^2 - 0.035306) - 0.008801 λ^2]
(*nx (λ) for LiIO3, λ in μm, ordinary index*)
ny[λ_] := Sqrt[3.415716 + 0.047031 / (λ^2 - 0.035306) - 0.008801 λ^2]
(*ny (λ) for LiIO3, λ in μm, ordinary index*)
nz[λ_] := Sqrt[2.918692 + 0.035145 / (λ^2 - 0.028224) - 0.003641 λ^2]
(*nz (λ) for LiIO3, λ in μm*)
```

```
λPump = 0.805 (*Ti:Sapphire laser wavelength in μm*)
ne[θ_] :=
ny[λPump/2] *
nz[λPump/2] /
(Sqrt[(ny[λPump/2] * Cos[θ * Pi/180])^2 +
(nz[λPump/2] * Sin[θ * Pi/180])^2])
```

```
θ[x_] := ArcSin[Sin[Pi*x/180]/ny[λPump]]*180/Pi
φ[y_] := ArcSin[Sin[Pi*(20-y)/180]/ny[λPump]]*180/Pi
ϕ[x_] := 51 + θ[x]
ψ[x_] := 51 - φ[x]
```

```
In[55]:= FindRoot[{ny[λPump] * (Sin[Pi ϕ[x]/180] + Sin[Pi
ψ[x]/180]) == 2ne[θ2HG]Sin[Pi θ2HG/180], ny[λPump] * (Cos[Pi
ϕ[x]/180] + Cos[Pi ψ[x]/180]) == 2ne[θ2HG]Cos[Pi
θ2HG/180]}, {x, 0}, {θ2HG, 46}]
```

```
Out[55]= {x → -1.28161, θ2HG → 45.0528}
```

(\*The crystal should be tilted to -1.28 degrees\*)

```
Out[56]= {x → -1.28161, θ2HG → 45.0528}
```

```
ArcSin[ne[45.0428*Pi/180]*Sin[(51-45.0528)*Pi/180]]*180/Pi
(*This is ArcSin[ne[θ2HG*Pi/180]*Sin[(51-θ2HG)*Pi/180]]*180/Pi*)
```

10.649

**10.649-1.28**  
(\*This is 10.649 - x\*)

9.369

(\*Expect the beam to exit the crystal at 9.4 degrees wrt the table\*)

```

(*ooe 2nd Harmonic Generation w/ LiIO3 upside down*)

(*Index ellipsoid for LiIO3*)
nx[λ_] := Sqrt[3.415716 + 0.047031 / (λ^2 - 0.035306) - 0.008801 λ^2]
(*nx (λ) for LiIO3, λ in μm, ordinary index*)
ny[λ_] := Sqrt[3.415716 + 0.047031 / (λ^2 - 0.035306) - 0.008801 λ^2]
(*ny (λ) for LiIO3, λ in μm, ordinary index*)
nz[λ_] := Sqrt[2.918692 + 0.035145 / (λ^2 - 0.028224) - 0.003641 λ^2]
(*nz (λ) for LiIO3, λ in μm*)

λPump = 0.805 (*Ti:Sapphire laser wavelength in μm*)
ne[θ_] :=
ny[λPump/2] *
nz[λPump/2] /
(Sqrt[(nz[λPump/2]*Cos[θ*Pi/180])^2 +
(ny[λPump/2]*Sin[θ*Pi/180])^2])

θ[x_]:=ArcSin[Sin[Pi*x/180]/ny[λPump]]*180/Pi
ϕ[y_]:=ArcSin[Sin[Pi*(20-y)/180]/ny[λPump]]*180/Pi
φ[x_]:=39 + θ[x]
ψ[x_]:=39 - ϕ[x]

FindRoot[{ny[λPump]*(Sin[Pi φ[x]/180]+Sin[Pi
ψ[x]/180])==2ne[θ2HG]Sin[Pi θ2HG/180], ny[λPump]*(Cos[Pi
φ[x]/180]+Cos[Pi ψ[x]/180])==2ne[θ2HG]Cos[Pi
θ2HG/180]}, {x,22}, {θ2HG,46}]
{x → 21.2816, θ2HG → 44.9472}

(*The crystal should be tilted to 21.3 degrees*)

ArcSin[ne[44.9472*Pi/180]*Sin[(-39+44.9472)*Pi/180]]*180/Pi
(*This is ArcSin[ne[θ2HG*Pi/180]*Sin[(-39+θ2HG)*Pi/180]]*180/Pi*)

11.6298

21.28-%
(*This is x - 11.629*)

9.65021

(*Expect the beam to exit the crystal at 9.6 degrees wrt the table*)

```

```

(*oeo sum-frequency generation (upconversion) w/ KTA right side up*)

(*Index ellipsoid for KTA*)
nx[λ]:= Sqrt[1.90713+1.23522/(1-(0.19692/λ)^2)-0.01025λ^2] (*nx(λ) for KTA, λ
in μm*)
ny[λ]:= Sqrt[2.15912+1.00099/(1-(0.21844/λ)^2)-0.01096λ^2] (*ny(λ) for KTA, λ
in μm*)
nz[λ]:= Sqrt[2.14786+1.29559/(1-(0.22719/λ)^2)-0.01436λ^2] (*nz(λ) for KTA, λ
in μm*)

λPL=3.17 (*peak wavelength for 173 sample, in μm*)
λPump=0.805 (*Ti:Sapphire laser wavelength in μm*)
λSFG=1/(1/λPL+1/λPump) (*Up-converted wavelength in μm*)

(*Extraordinary index for Pump wavelength for angle, θ, in crystal relative to
z-axis*)
ne[θ]:= nx[λPump]*nz[λPump]/(Sqrt[(nx[λPump]*Cos[Pi*θ/180])^2 +
(nz[λPump]*Sin[Pi*θ/180])^2])

FindRoot[{ny[λPL]Cos[.82 + ArcSin[Sin[.35 - ArcSin[Sin[Pi*(47-
x)/180]*ne[x]]]/ny[λPump]]]/λPL + ne[x]Cos[Pi*x/180]/λPump ==
ny[λSFG]Cos[Pi*θSFG/180]/λSFG, ny[λPL]Sin[.82 + ArcSin[Sin[.35 -
ArcSin[Sin[Pi*(47-x)/180]*ne[x]]]/ny[λPump]]]/λPL + ne[x]Sin[Pi*x/180]/λPump
== ny[λSFG]Sin[Pi*θSFG/180]/λSFG}, {x, 30}, {θSFG, 40}]

{x → 45.1932, θSFG → 47.3292}

(*x is θPumpCry2, θSFG is angle wrt x-axis in crystal*)

θPLin[y]:= 20 - ArcSin[Sin[Pi*(47-y)/180]*ne[y]]*180/Pi
(*θPLin is θPLin[θPumpCry2]*)

θPLin[45.19]
16.6755

(*Crystal should be tilted at 16.68 degrees*)
Ψ[z]:= ArcSin[ny[λSFG]Sin[Pi*(z-47)/180]]*180/Pi
(*This is Ψ[θSFG]*)

16.675 - Ψ[47.329]
(*This is θPLin[θPumpCry2] - Ψ[θSFG]*)
```

16.0785

(\*λSFG beam will exit the crystal at 16.08 degrees wrt the table,
ie. normal to the crystal's surface\*)

```

(*ceo sum-frequency generation (upconversion) w/ KTA upside down*)

(*Index ellisoid for KTA*)
nx[λ_] := Sqrt[1.90713+1.23522/(1-(0.19692/λ)^2)-0.01025λ^2] (*nx(λ) for KTA, λ
in μm*)
ny[λ_] := Sqrt[2.15912+1.00099/(1-(0.21844/λ)^2)-0.01096λ^2] (*ny(λ) for KTA, λ
in μm*)
nz[λ_] := Sqrt[2.14786+1.29559/(1-(0.22719/λ)^2)-0.01436λ^2] (*nz(λ) for KTA, λ
in μm*)

λPL=3.17 (*peak wavelength for 173 sample, in μm*)
λPump=0.805 (*Ti:Sapphire laser wavelength in μm*)
λSFG=1/(1/λPL+1/λPump) (*Up-converted wavelength in μm*)

(*Extraordinary index for Pump wavelength for angle, θ, in crystal relative to z-
axis*)
ne[θ_] := nx[λPump]*nz[λPump]/(Sqrt[(nz[λPump]*Cos[Pi*θ/180])^2 +
(nx[λPump]*Sin[Pi*θ/180])^2])

FindRoot[{ny[λPL]*Cos[.75 + ArcSin[Sin[.35 - ArcSin[Sin[Pi*(43-
x)/180]*ne[x]]]/ny[λPump]]]/λPL + ne[x]*Cos[Pi*x/180]/λPump ==
ny[λSFG]*Cos[Pi*θSFG/180]/λSFG, ny[λPL]*Sin[.75 + ArcSin[Sin[.35 -
ArcSin[Sin[Pi*(43-x)/180]*ne[x]]]/ny[λPump]]]/λPL + ne[x]*Sin[Pi*x/180]/λPump ==
ny[λSFG]*Sin[Pi*θSFG/180]/λSFG}, {x, 30}, {θSFG, 40}]

{x → 44.7381, θSFG → 46.8566}

(*x is θPumpCry2, θSFG is angle wrt z-axis in crystal*)

θPLin[y_] := 20 - ArcSin[Sin[Pi*(43 - y)/180]*ne[y]]*180/Pi
(*θPLin is θPLin[θPumpCry2]*)

θPLin[44.7381]

23.1922

(*Crystal should be tilted at 23.1922 degrees*)
Ψ[z_] := ArcSin[ny[λSFG]*Sin[Pi*(z - 43)/180]]*180/Pi
(*This is Ψ[θSFG]*)

23.1922 - Ψ[46.85]
(*This is θPLin[θPumpCry2] - Ψ[θSFG]*)
```

16.2004

(\*λSFG beam will exit the crystal at 16.2 degrees wrt the table,
ie. normal to the crystal's surface\*)

## **Appendix B-Mirror Alignment Procedure**

This appendix will present the alignment procedure for the off-axis parabolic mirrors used in the experimental setup. The alignment of these mirrors is the most critical aspect of the setup and, although there was some literature regarding the alignment of one parabolic mirror Lee (1992), there was no literature on aligning one parabolic mirror to another. The majority of the time spent on the setup up was allocated on developing such an alignment procedure.

### **B.1 First Time Alignment Procedure**

The reader is urged to become familiar with the position of parabolic mirrors 1 and 2, and the orientation of the X and Y axes on the table indicated on Figure B-1. The reader is also expected how to expand a HeNe laser using Jodon beam expander. The following procedure is used if the mirrors have been completely removed from the setup.

The height of the entire experiment is determined by the height of the pinhole mounted in the rotation stage. Because of this, we begin aligning the mirrors by working backwards, that is, we will begin by aligning mirror 1 first to the pinhole mounted in the rotation stage.

#### **B.1.1 Aligning Mirror 1**

We begin by expanding a HeNe laser using a Jodon beam expander, collimating it and focusing it through the pinhole using a pair of plano-concave lenses as indicated in Figure B-1. As the HeNe laser exits the pinhole, it acts as a point source emitting in some solid angle. Replace mirror 1 and orient it so that the HeNe reflects off of it in the Y-direction. Secure mirror 1.

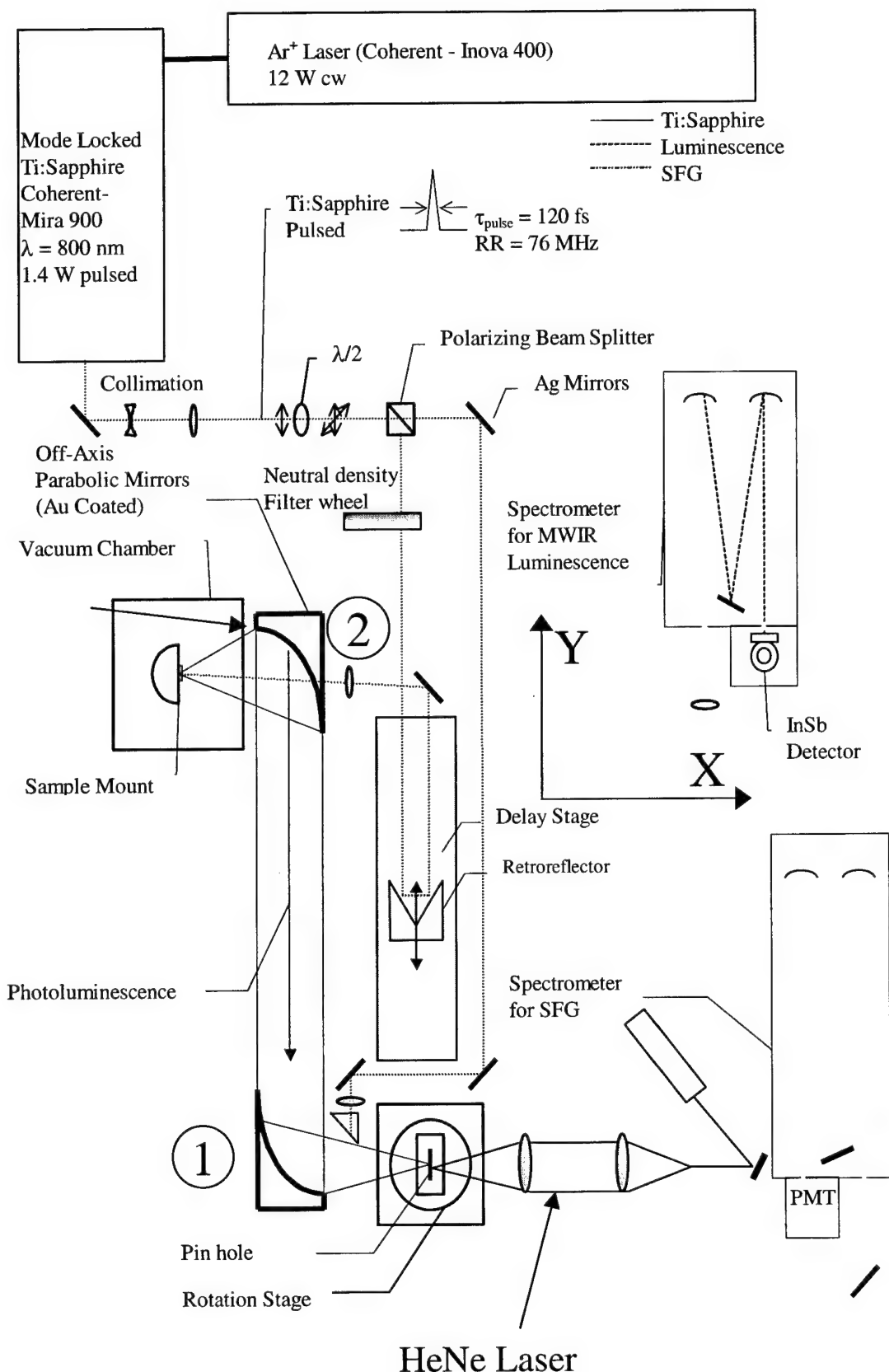


Figure B-1: Experimental setup indicating mirrors 1 and 2, and X- Y- axis.

Level the HeNe with respect to the table top and align it so that it is parallel with the Y-axis. Intercept the HeNe near mirror 1 with a series of flat mirrors so that the HeNe is allowed to propagate a large distance, for example across the room. After the HeNe has propagated a large distance, place in a screen so that it can be viewed. The HeNe is probably not circular. Adjust the x-y-z manipulator that the mirror sits on so that the HeNe is circular. Check to see if the HeNe is still level and parallel to the Y-axis. It probably is not. Adjust the set-screws in the base of the mirror mount so that the HeNe is level and aligned to the Y-axis. The goal is to get the HeNe level with the table, aligned to the Y-axis, and circular after propagating a large distance. After a few iterations of the steps above, the goal can be accomplished.

### **B.1.2 Aligning Mirror 2**

Replace mirror 2 and secure it. With the Ti:Sapphire laser on, focus it on the surface of the cold finger, which sits inside the vacuum chamber. Collect the scatter of the Ti: with mirror 2 and direct it along the Y-axis of the table, toward mirror 1, and level the scattered Ti: to the table. Using a similar set up as in section B.1.1, propagate the scattered Ti: over a large distance and view it. As in section B.1.1, get the scattered Ti: level with the table, aligned to the Y-axis, and in the shape of a two-inch-diameter circle after propagating it.

Next, check to see if the scatter of the Ti: is centered on mirror 1. If not, collectively adjust the vacuum chamber and mirror 2 appropriately until the scatter is centered on mirror 1.

Finally, adjust the x-y-z manipulator of mirror 1 so that the scatter of the Ti: transmits through the pinhole mounted in the rotation stage by mounting a screen behind the pinhole.

## B.2 Daily Alignment Procedure

For the daily alignment procedure, simply perform the procedure outlined in section B.2.1 but omit the portions where you level the scatter and align the scatter to the Y-axis. The scatter should remain level and aligned to the Y-axis as long as the set-screws in the base of mirror 2 are not adjusted after the First Time Alignment is performed.

## B.3 Tricks and Voodoo

The following are the tricks that aid in getting an upconverted signal.

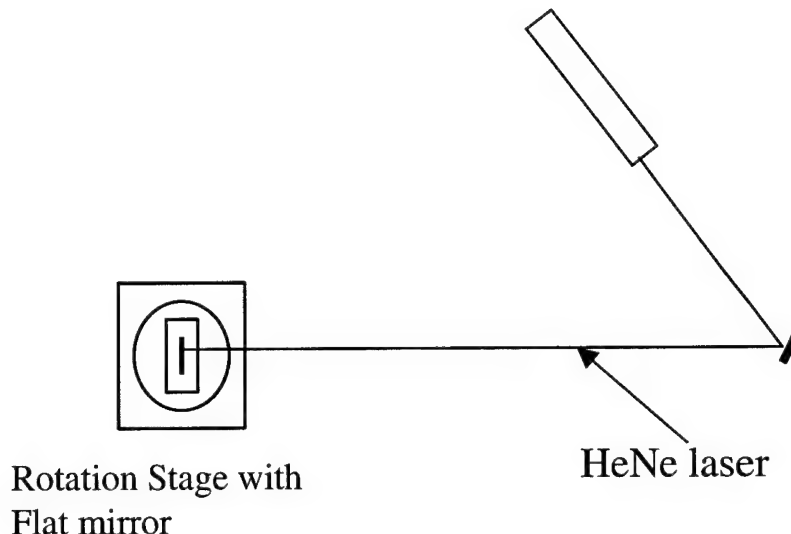


Figure B-1: HeNe laser illuminating a flat mirror.

### B.3.1 Collection Optic Placement

Remove all optics used in expanding the HeNe in the previous sections. Also, remove the pinhole from the rotation stage and replace it with a flat mirror (special mirror and mirror mount is supplied).

At this point, the HeNe should not be encountering any optics when it reaches the flat mirror in the rotation stage (Figure B-1).

Next, level and align the HeNe to the X-axis. Then, center an iris to the HeNe and rotate the stage so that the reflection off the mirror follows the same path as the oncoming HeNe. Set the stage to zero degrees. Now, every angle will be measured with respect to the X-axis. Since most upconverted beams exit the KTA crystal at around  $16^\circ$  with respect to the X-axis, rotate the stage to  $8^\circ$ . This puts the reflected HeNe at  $16^\circ$  on the table. Level the HeNe. Now center two irises on the HeNe as indicated in Figure B-2 and lock them down. These irises are now markers to help place the collection optic in place.

Now remove the flat mirror and replace it with the pinhole. Also, replace the optics used to expand the HeNe and focus the HeNe back through the pin hole as indicated in Figure B-3.

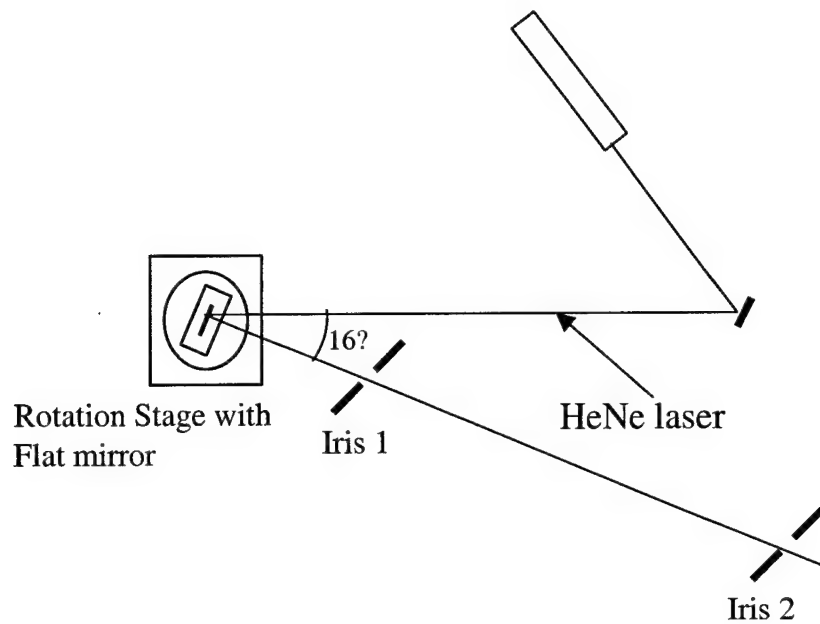


Figure B-2: HeNe at 16 degrees with two irises.

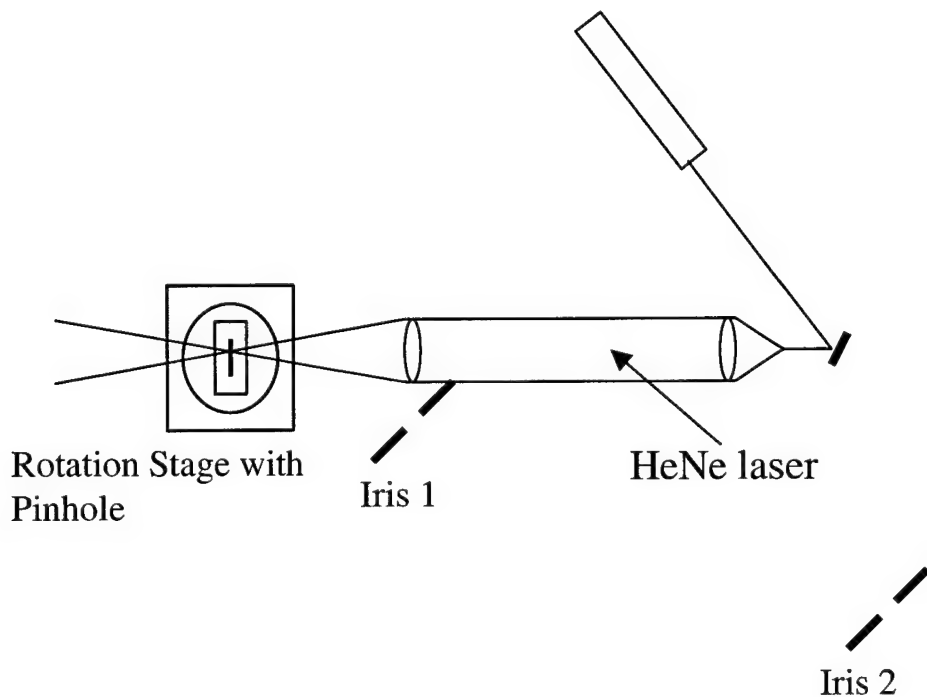


Figure B-3: Expanded HeNe through pinhole.

Now, remove the pinhole and replace it with the flat mirror again. Rotate the stage until the HeNe reflecting off the flat mirror is centered on the iris 1. Ignore what the read-out says on the stage controller. Then place in the collection optic so that the transmitted HeNe is centered on the iris 2 as in Figure B-5.

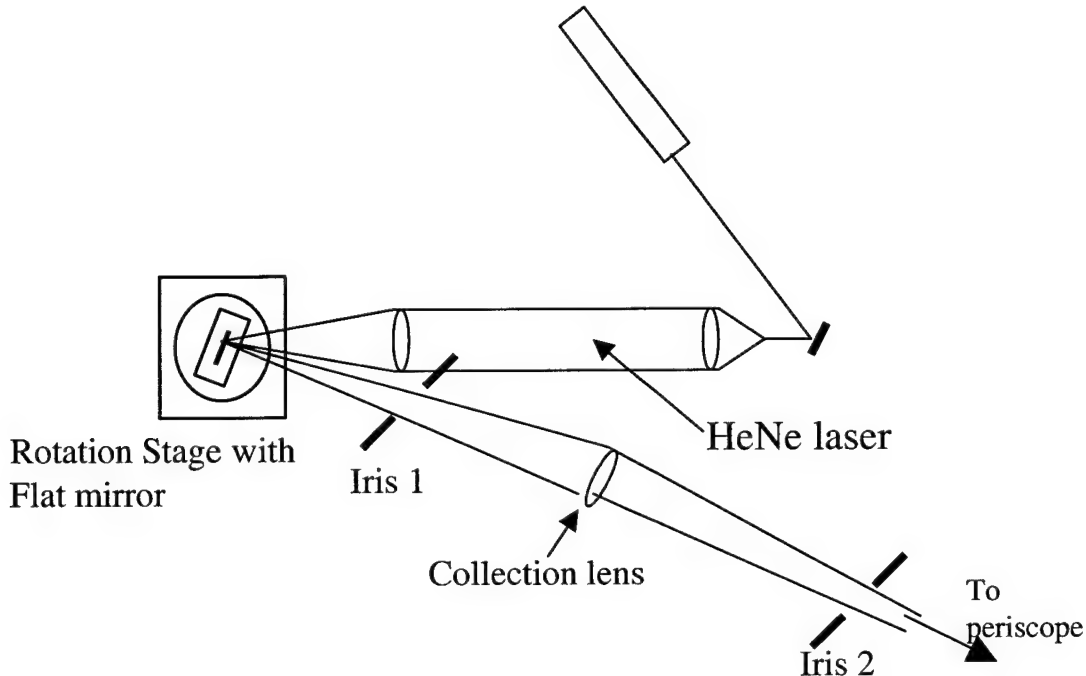


Figure B-4: HeNe imitating upconverted beam.

Along with the periscope, guide the HeNe into the slits of the Spex monochrometer by adjusting the collection lens back and fourth. Right after the HeNe leaves the second mirror of the periscope, make sure that the HeNe is level with the table.

### B.3.2 Beam Overlap and Zero Path Length

With the scatter of the Ti: off the cold finger going through the pinhole that is mounted in the rotation stage, position the pump beam through the pinhole as well. Remove the pinhole and replace it with the LiIO<sub>3</sub> crystal mounted upside down (The mount is indicated as such). The pinhole and LiIO<sub>3</sub> crystal do not ‘sit’ at the same place when mounted in the stage. In order to place the crystal at the same spot as the pinhole, you have to translate the stage, using the z-micrometer (See Figure B-5), a difference of 0.64 mm.

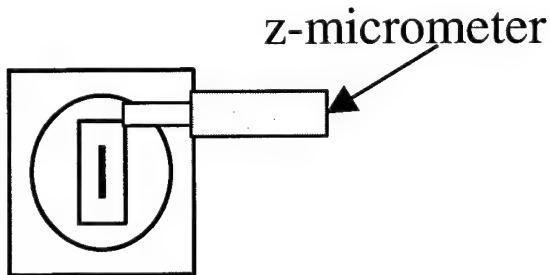


Figure B-5: Close up of rotation stage showing z-micrometer.

Rotate the stage to the specified angle given by the Mathematica file for the LiIO<sub>3</sub> crystal being upside down. Turn off all the lights and put on the safety goggles. Run the Lab Windows program used in the upconversion experiment. Using the program, translate the delay stage back and fourth until you see a flash of purple light. That flash is the Second Harmonic Generated Beam. Position the delay stage so that the SHG beam is always visible and set the delay stage to zero in the Lab Windows program.

### **B.3.3 Sample Placement**

Once the mirrors are aligned and the scatter of the Ti: off of the cold finger is going through the pinhole, the surface of the sample being investigated must be placed where the cold finger is currently sitting. First, translate the chamber left or right, i.e. along the Y-axis, and up or down so that the Ti: is illuminating the sample. Twist the chamber so that a small portion of the Ti:, reflecting off the surface of the sample, is caught by the left-hand edge of mirror 2. Now, while viewing the screen mounted behind the pinhole, translate the chamber back until you can see the reflected portion of the Ti: on the screen. The sample is now in the position for performing upconversion.

### **B.3.4 Finding the Upconversion Signal**

With the sample cooled and at the right position, the PMT cooled, and all other equipment on, remove the pinhole and replace it with the KTA crystal. Much like the case with the LiIO<sub>3</sub> crystal, the KTA crystal is not at the same place as the pinhole was. Translate the delay stage to the positive 50 ps position, not allowing it to move afterward. Rotate the stage to the angle given by the Mathematica file for the KTA crystal being right side up. While the experiment is running, slowly translate the KTA crystal, using the z-micrometer, until the counts begin to increase. Adjust the z-micrometer until the counts max out. Congratulations, you have upconverted photons!

### **B.3.4 Tweaking**

There are four things that can be tweaked in order to get a better upconverted signal. The first is the lens that focuses the pump beam just before the pinhole. That lens can be adjusted so that a better overlap can be achieved between the PL and pump beam. The second is the angle of the rotation stage. This can also be adjusted to achieve

a stronger upconverted signal. The third is the z-micrometer on the rotation stage. The fourth is the monochrometer setting. This should also be adjusted to see if the counts can be increased.

## Bibliography

- Almuneau, G. and F. Genty and A. Wilk and P. Grech and A. Joullie and L. Chusseau, "GaInSb/AlGaAsSb Strained Quantum Well Semiconductor Lasers for 1.55  $\mu\text{m}$  Operation," *Semicond. Sci. Technol.* 14: 89-92 (1999).
- Choi, H.K. and G.W. Turner and Z.L. Liau, "2.2  $\mu\text{m}$  of GaInAsSb/AlGaAsSb," *Appl. Phys. Lett.* 65:2251-2253 (1996).
- Chow, D.H. and R. H. Miles and T.C. Hasenberg and A. R. Kost and Y. H. Zhang, and H. L. Dunlap and L. West, "Mid-Wave Infrared Diode Lasers Based on GaInSb/InAs and InAs/AlSb Superlattices," *Appl. Phys. Lett.* 67 (25), (December 1995).
- Cooley, W.T. *Measurement of Ultrafast Carrier Recombination Dynamics in Mid-Infrared Semiconductor Laser Material*, Dissertation, Air Force Institute of Technology (December 1997).
- Hausser, S. and G. Fuchs and A. hangleiter and K. Streubel and W.T. Tsang, "Ajuger Recombination I Bulk and Quatum Well InGaAs," *Appl. Phys. Lett.* 56(10):913-915(March 1990).
- Heyen, E.T. and M. hagerott and A.V. Nurmikko and D.L. Partin, "Radiative Recombination in PbTe Quantum Wells," *Appl. Phys. Lett.* 54(7), (February 1989).
- Kuang, G. K. and G. Bohm and M. Grau and G. Rosel and R. Meyer andM. C. Amann, "2.12  $\mu\text{m}$  InGaAs-InGaAlAs-InP Diode Lasers Grown in Solid-Source Molecular-Beam Epitaxy," *Appl. Phys. Lett.* 77 (8), (August 2000).
- Lane, B. and D. Wu and A. Rybaltowski and H. Yi and J. Diaz and M. Razeghi, "Compressively Strained Multiple quantum Well InAsSb Lasers emitting at 3.6  $\mu\text{m}$  Grown by Metal-Organic Chemical Vapor Deposition," *appl. Phys. Lett.* 70 (4), (January 1997).
- Lee, Yeon H., "Alignment of an Off Axis parabolic Mirror with Two parallel He-Ne Laser Beams," *Optical Engineering* 31(11), 2287-2292 (November 1992).
- Marciniak, M.A. Optical Characterizaiton of MBE-Grown InAs<sub>1-x</sub>Sb<sub>x</sub> Semiconductros on GaSb Substrate, Dissertation, Air Force Institute of Technology (August 1995).
- Mahr, H. and M.D. Hirsch, "An Optical Up-Conversion Light Gate with Picosecond Resolution," *Optical Communications*, 13 (2): 96 (February 1975).
- McCaheon, S.W. and A. A. Anson and D.J. Jang and M..E. Flatte and Thomas F. Boggess and D. H. Chow and T.C. Hasenberg and C.H. Grein, "Carrier Recombinaiton Dynamics in a (GaInSbInAs)/AlGaSb Superlattice Multiple Quantum Well," *Appl. Phys. Lett.* 68(15) (April 1996).

Oohashi, H. and T. Hirono and S. Seki and H. Sugiura and J. Nakano and M. Yamamoto and Y. Tohmori and K. Yokoyama, “1.3  $\mu\text{m}$  InAsP Compressively Strained Multiple-Quantum-Well Lasers for high-Temperature Operation,” *J. Appl. Phys.* 77 (8), (April 1995).

Qian, S. and Jie Song and yufen Li, “Nonradiative, Radiative Recombinaion and Trapping Processes in the InGaAs/GaAs Single Quantum Wells,” *Ultrafast Pulse Gerneration and Spectroscopy*, SPIE Vol. 1861:363-369 (1993).

Shah, Jagdeep “Ultrafast Luminescence Spectroscopy Using Sum Frequency Generation,” *IEEE Journal of Quantum Electroncis*, QE-24(2):276-288 (February 1988).

Snow, P.A., and P. Maly and D.J. Westland and J.F. Ryan, “Picosecond Photoluminescence Measurements of Hot Carrier Relaxation and Auger Recombination in GaSb,” *Solid-State Electronics* 32(12):1485-1489 (1989).

Turner, G.W. and H. K. Choi and H.Q. Le, “Growth of InAsSb quantum wells for long-wavelength ( $\sim 4 \mu\text{m}$ ) lasers,” *J. Vac. Sci. Technol. B* 13(2), (Mar/Apr 1995).

Zhang, L. and Thomas F. Boggess and D. G. Deppe and D. L. Huffaker and O. B. Shchekin and C. Cao, “Dynamic Response of 1.3- $\mu\text{m}$ -Wavelength InGaAs/GaAs Quantum Dots,” *Appl. Phys. Lett.* 76 (10), (March 2000).

## **Vita**

Michael Reynaldo McKay was born on a bright and sunny day in the middle of August in the year of 1975 in the small but quaint town of Bradenton, Florida. The villagers of this small community rejoiced at the birth of this child because it meant the beginning of a plentiful harvest. At the age of two, this child found Zebulon uneventful and longed for the excitement that he had heard about in the stories of the Southwest cities told by the elders that frequented the local tavern. After moving to the booming, boarder city of El Paso, Texas, this child grew to a young man and attended high school and college, where he learned the ways of the great masters such as Tesla, Faraday, and Newton. Realizing that he was drawn to a higher calling, he searched the land for an institution where he could continue his studies of the masters. He eventually found such an environment at the Air Force Institute of Technology. And on June 8, 2001, Michael joined the ranks of the elite when he received his Master's degree in Engineering Physics. The villagers of that small town of Bradenton still sing songs of the epic journeys of that child that they had known so long ago.

## REPORT DOCUMENTATION PAGE

Form Approved  
OMB No. 0704-0188

The public reporting burden for this collection of information is estimated to average 1 hour per response, including the time for reviewing instructions, searching existing data sources, gathering and maintaining the data needed, and completing and reviewing the collection of information. Send comments regarding this burden estimate or any other aspect of this collection of information, including suggestions for reducing the burden, to Department of Defense, Washington Headquarters Services, Directorate for Information Operations and Reports (0704-0188), 1215 Jefferson Davis Highway, Suite 1204, Arlington, VA 22202-4302. Respondents should be aware that notwithstanding any other provision of law, no person shall be subject to any penalty for failing to comply with a collection of information if it does not display a currently valid OMB control number.

**PLEASE DO NOT RETURN YOUR FORM TO THE ABOVE ADDRESS.**

1. REPORT DATE (DD-MM-YYYY) 01-06-2001			2. REPORT TYPE Master's Thesis		3. DATES COVERED (From - To) Nov 1999-May 2001	
4. TITLE AND SUBTITLE Time-Resolved Photoluminescence of InAs/GaInSb Quantum Well Lasers			5a. CONTRACT NUMBER			
			5b. GRANT NUMBER SN-AFIT-00-05			
			5c. PROGRAM ELEMENT NUMBER			
6. AUTHOR(S) Michael R. McKay			5d. PROJECT NUMBER ENR 01-414		5e. TASK NUMBER	
			5f. WORK UNIT NUMBER			
7. PERFORMING ORGANIZATION NAME(S) AND ADDRESS(ES) Air Force Institute of Technology Graduate School of Engineering and Management (AFIT/ENP)					8. PERFORMING ORGANIZATION REPORT NUMBER AFIT/GAP/ENP/01J-02	
9. SPONSORING/MONITORING AGENCY NAME(S) AND ADDRESS(ES) DAFGSI Attn: Dr. Frank Moore 3155 Research Boulevard, Suite 205					10. SPONSOR/MONITOR'S ACRONYM(S)	
					11. SPONSOR/MONITOR'S REPORT NUMBER(S)	
12. DISTRIBUTION/AVAILABILITY STATEMENT APPROVED FOR PUBLIC RELEASE; DISTRIBUTION UNLIMITED.						
13. SUPPLEMENTARY NOTES						
14. ABSTRACT In the world of semiconductor photonic device fabrication, one important objective may be to extract as much light as possible from the device. In these devices, photons are created when electrons recombine with holes by transitioning from a high-energy state to a lower one. Unfortunately, electron-hole recombination does not always result in the formation of a photon. There are three basic types of recombination: the first results in the formation of a photon and is called radiative recombination; and the second and third, known as Shockley-Read-Hall and Auger recombination, result in the heating of the device and do not produce photons and are therefore called non-radiative recombination. All three processes occur simultaneously in a device, and either a radiative or non-radiative recombination coefficient can be associated with the relative rate of each. The lifetime of an electron in a high-energy state is so small, on the order of nanoseconds, that there is no way to measure these coefficients directly. However, sum frequency generation is a technique to indirectly measure these coefficients by taking advantage of the speed of light to resolve these processes in time. From the resulting data, these recombination coefficients can be extracted.						
15. SUBJECT TERMS Photoluminescence (PL), Sum Frequency Generation (SFG), Second Harmonic Generation (SHG), Upconversion, Quantum Well Lasers, Gallium Indium Antimonide (GaInSb)						
16. SECURITY CLASSIFICATION OF: a. REPORT U			17. LIMITATION OF ABSTRACT UU	18. NUMBER OF PAGES 67	19a. NAME OF RESPONSIBLE PERSON Lt. Col. M.A. Marciniak	
					19b. TELEPHONE NUMBER (Include area code) (937)255-3636 x4529	

## INSTRUCTIONS FOR COMPLETING SF 298

**1. REPORT DATE.** Full publication date, including day, month, if available. Must cite at least the year and be Year 2000 compliant, e.g. 30-06-1998; xx-06-1998; xx-xx-1998.

**2. REPORT TYPE.** State the type of report, such as final, technical, interim, memorandum, master's thesis, progress, quarterly, research, special, group study, etc.

**3. DATES COVERED.** Indicate the time during which the work was performed and the report was written, e.g., Jun 1997 - Jun 1998; 1-10 Jun 1996; May - Nov 1998; Nov 1998.

**4. TITLE.** Enter title and subtitle with volume number and part number, if applicable. On classified documents, enter the title classification in parentheses.

**5a. CONTRACT NUMBER.** Enter all contract numbers as they appear in the report, e.g. F33615-86-C-5169.

**5b. GRANT NUMBER.** Enter all grant numbers as they appear in the report, e.g. AFOSR-82-1234.

**5c. PROGRAM ELEMENT NUMBER.** Enter all program element numbers as they appear in the report, e.g. 61101A.

**5d. PROJECT NUMBER.** Enter all project numbers as they appear in the report, e.g. 1F665702D1257; ILIR.

**5e. TASK NUMBER.** Enter all task numbers as they appear in the report, e.g. 05; RF0330201; T4112.

**5f. WORK UNIT NUMBER.** Enter all work unit numbers as they appear in the report, e.g. 001; AFAPL30480105.

**6. AUTHOR(S).** Enter name(s) of person(s) responsible for writing the report, performing the research, or credited with the content of the report. The form of entry is the last name, first name, middle initial, and additional qualifiers separated by commas, e.g. Smith, Richard, J, Jr.

**7. PERFORMING ORGANIZATION NAME(S) AND ADDRESS(ES).** Self-explanatory.

**8. PERFORMING ORGANIZATION REPORT NUMBER.** Enter all unique alphanumeric report numbers assigned by the performing organization, e.g. BRL-1234; AFWL-TR-85-4017-Vol-21-PT-2.

**9. SPONSORING/MONITORING AGENCY NAME(S) AND ADDRESS(ES).** Enter the name and address of the organization(s) financially responsible for and monitoring the work.

**10. SPONSOR/MONITOR'S ACRONYM(S).** Enter, if available, e.g. BRL, ARDEC, NADC.

**11. SPONSOR/MONITOR'S REPORT NUMBER(S).**

Enter report number as assigned by the sponsoring/monitoring agency, if available, e.g. BRL-TR-829; -215.

**12. DISTRIBUTION/AVAILABILITY STATEMENT.** Use agency-mandated availability statements to indicate the public availability or distribution limitations of the report. If additional limitations/ restrictions or special markings are indicated, follow agency authorization procedures, e.g. RD/FRD, PROPIN, ITAR, etc. Include copyright information.

**13. SUPPLEMENTARY NOTES.** Enter information not included elsewhere such as: prepared in cooperation with; translation of; report supersedes; old edition number, etc.

**14. ABSTRACT.** A brief (approximately 200 words) factual summary of the most significant information.

**15. SUBJECT TERMS.** Key words or phrases identifying major concepts in the report.

**16. SECURITY CLASSIFICATION.** Enter security classification in accordance with security classification regulations, e.g. U, C, S, etc. If this form contains classified information, stamp classification level on the top and bottom of this page.

**17. LIMITATION OF ABSTRACT.** This block must be completed to assign a distribution limitation to the abstract. Enter UU (Unclassified Unlimited) or SAR (Same as Report). An entry in this block is necessary if the abstract is to be limited.